

# Beyond the Local Volume: Surface Densities of Ultracool Dwarfs in Deep HST/WFC3 Parallel Fields

CHRISTIAN AGANZE,<sup>1</sup> ADAM J. BURGASSER,<sup>1</sup> MATHEW MALKAN,<sup>2</sup> CHIH-CHUN HSU,<sup>1</sup> CHRISTOPHER A. THEISSEN,<sup>1</sup> DANIELLA C. BARDALEZ GAGLIUFFI,<sup>3</sup> RUSSEL RYAN,<sup>4</sup> AND BENNE HOLWERDA<sup>5</sup>

<sup>1</sup>*Department of Physics, University of California, San Diego, CA 92093, USA*

<sup>2</sup>*Department of Physics & Astronomy, University of California, Los Angeles, CA 90095, USA*

<sup>3</sup>*Department of Astrophysics, American Museum of Natural History, Central Park West at 79th Street, NY 10024, USA*

<sup>4</sup>*Space Telescope Science Institute, 3700 San Martin Dr., Baltimore, MD 21218*

<sup>5</sup>*Department of Physics and Astronomy, 102 Natural Science Building, University of Louisville, Louisville KY 40292, USA*

## ABSTRACT

Ultracool dwarfs (UCDs) of the L, T, and Y spectral classes are the lowest-mass and coldest objects in the Milky Way. Like stars, they are tracers of Galactic structure and star-formation history, while the cooling of substellar UCDs provide additional probes for galactic archeology and chemical evolution. Wide-field optical and infrared surveys have uncovered thousands of UCDs, but primarily in the immediate solar neighborhood ( $d < 100$  pc). To push to larger distances, we have searched over  $0.5 \text{ deg}^2$  of the WFC3 Infrared Spectroscopic Parallel Survey and the 3D-HST parallel survey with low-resolution near-infrared spectra. We report the discovery of 168 M7-T9 and T dwarfs with spectro-photometric distances up to  $\sim 2$  kpc for L dwarfs and  $\sim 400$  pc for T dwarfs. We model the number density distribution with population simulations incorporating various assumptions of the intrinsic MF and birth rates, accounting for UCD evolutionary models and Galactic structure. We under-predict the number den-

sity of T dwarfs in our simulation, reflecting a larger scale height ( $h > 1000$  pc) for these old populations. Future infrared sky surveys conducted with the James Webb Space Telescope (JWST) or the Euclid mission will put finer constraints on the true scale height of UCDS. We predict that Euclid will yield  $\sim 10^4$  L dwarfs and  $\sim 10^4$  T dwarfs spectra in the Euclid South and Euclid Fornax fields alone for a limiting magnitude of  $J=24$ , providing enough statistics to fully characterize UCDs in the Galactic context.

## 1. INTRODUCTION

The structure and evolution of the Milky Way is largely inferred from heterogeneous spatial and kinematic distributions of its stars. Star-count data show that the overall structure conforms to a younger population fit to one or more exponential disks and an older population fit to a power-law or oblate spheroid (de Vaucouleurs & Pence 1978; Bahcall & Soneira 1981; Jurić et al. 2008); and models show that the disk started forming stars 8–11 Gyr ago, while the halo star-formation history dates to 10–13 Gyr ago from possible multiple merger events. Hence, halo stellar populations contain stars with ages comparable to the age the universe (Leggett et al. 1998; Tolstoy et al. 2009; Haywood et al. 2013). Questions relating to the formation and evolution of the Galaxy through its stars constitute the field of Galactic archeology (Freeman 1987; Ivezić et al. 2012), which, through the usage of large sky surveys (e.g the Sloan Digital Sky Survey, York & Others 2000), has enabled a 6-dimensional depiction of the Galaxy. The Gaia mission (Gaia Collaboration et al. 2018) has recently contributed to our understanding of the Milky Way. Some of the notable discoveries include major merger events that formed the inner stellar halo and thick disk (Gaia-Enceladus/Gaia sausage: Helmi et al. 2018; Belokurov et al. 2018; Myeong et al. 2018; Gallart et al. 2019, and the Sequoia event: Myeong et al. 2018, 2019), the discovery and characterization of hypervelocity stars (Boubert et al. 2018), stellar streams as probes of the Galactic potential and dark matter profile (Boubert et al. 2018; Malhan et al. 2018; Koppelman et al. 2019). The Gaia mission has also enabled the discovery of substructure in the solar neighborhood in the galactic disk caused by phase mixing in velocity space, from possible interactions with the spiral structure of the Galaxy (Antoja et al. 2018).

Ultracool dwarfs (UCDs;  $M \lesssim 0.1 M_{\odot}$ ,  $T_{eff} \lesssim 3000\text{K}$ ; Kirkpatrick 2005) provide a new approach for studying the Galaxy (Burgasser 2004; Ryan et al. 2017). They constitute  $\sim 50\%$  of the total number of stars and they are abundant in every environment in the Galaxy (Cruz et al. 2007; Chabrier & Baraffe 2000; Burrows et al. 2001; Bochanski et al. 2010). Stellar UCDs have lifetimes far in excess of the age of the Galaxy ( $> 10^3$  Gyr, Laughlin et al. 1997), while substellar UCDs (brown dwarfs) do not fuse hydrogen and hence cool down with time (Hayashi & Nakano 1963). They have distinct spectra shaped by strong molecular absorption bands that are highly sensitive to temperature, surface gravity and metallicity. The evolution of UCDs provides potential age diagnostics that have already been exploited in stellar cluster studies (Basri 1998; Luhman & Mamajek 2012; Martin et al. 2017) and searches of young moving groups near the Sun (Lopez-Santiago et al. 2006, Gagné et al. 2015, Mamajek 2015, Faherty et al. 2018).

UCDs have historically been discovered in red optical and infrared sky surveys (DENIS: Delfosse et al. 1999, SDSS: Schmidt et al. 2010, 2014; Theissen et al. 2017, VISTA: Lodieu et al. 2012; Downes et al. 2014; 2MASS: Cruz et al. 2007; Kirkpatrick et al. 2010, WISE: Kirkpatrick et al. 2011; Cushing et al. 2011, UKIDSS: Marocco et al. 2015; Day-Jones et al. 2013; Burningham et al. 2013; Skrzypek et al. 2016, CFHT-LAS: Reyle et al. 2010, Gaia: Reylé 2018; Kiman et al. 2019) but due to their intrinsic faintness, these samples are distance limited ( $\leq 100\text{pc}$ ). Hence, efforts to measure the UCD luminosity function have focused on compiling volume-limited samples within 20–25 pc of the sun (Cruz et al. 2007; Metchev et al. 2008; Reyle et al. 2010; Kirkpatrick et al. 2019; Bardalez Gagliuffi et al. 2019). Wide-field surveys provide large samples of UCDs, however, these studies do not effectively probe Galactic structure, nor the oldest UCD populations that formed in the early metal-poor Galaxy which may have had a distinct initial mass function (Bate et al. 2002; Bromm & Loeb 2003; Bate et al. 2003). To investigate the complete UCD population of the Galaxy these scenarios, it is necessary to identify UCDs populations beyond the solar neighborhood and further into the thick disk and halo of the Milky Way.

Deep pencil-beam imaging surveys provide a novel approach to use star-count data in characterization of UCD populations beyond the local volume. A common approach is to use photometric

selections cuts anchored to known sample. Early work by [Gould et al. \(1997\)](#) conducted an M-dwarf number counts to measure the halo luminosity function of the Hubble Space Telescope’s Wide Field Camera 2 (HST-WFC2) and Planetary Camera (PC1) Deep Fields. They found 47 M dwarfs with  $M_V > 13.5$ , and the distribution was consistent with a power law the mass function that turns at  $M \sim 0.6 M_\odot$  from  $\alpha = -1$  to  $\alpha = 0.44$ . Subsequent studies by [Kerins \(1997\)](#); [Chabrier & Mera \(1997\)](#) concluded that the contribution of low-mass stars ( $M \sim 0.3 M_\odot$ ) to the halo luminosity function is less than 1%. [Ryan Jr. et al. \(2005\)](#) searched 15 deep parallel fields from the Hubble Space Telescope star-count optical data obtained with the ACS instrument, selected by their i-z colors. They estimated a scale of  $\sim 350$  pc for L & T dwarfs. Later work by [Ryan et al. \(2011\)](#) found 17 late M, L and T dwarfs in  $231.90 \text{ arcmin}^2$  of WFC3 imaging of the GOODS fields using a combination of wide and narrow-band filter colors. They estimated a disk scale height of  $290 \pm 39$  pc consistent with work by [Pirzkal et al. \(2005\)](#). In addition to poor estimate of spectral types, these samples were contaminated with various non-stellar sources that could not be identified in the absence of spectral information. To push towards a larger and pure sample, [Holwerda et al. \(2014\)](#) identified 274 in  $227 \text{ arcmin}^2$  M-dwarfs (to a limiting magnitude F125W=25) from the HST-WFC3 Brightest of Re-ionizing Galaxies (BoRG, [Pirzkal et al. 2009](#)) survey, using an optical and near-infrared colors and determined their spectral types using V-J color-M-dwarf subtype relation ([Pirzkal et al. 2009](#)). They found a slightly higher density of M-dwarfs identified in the Northern fields compared to the Southern Fields, and a disk scale-height of 0.3–4 kpc with a dependence on subtype. The overall M-dwarf scale height was  $\sim 600$  pc, a number that is much larger than previous estimates mostly due to large uncertainties in the fit. [Van Vledder et al. \(2016\)](#) reanalyzed these data using a Markov Chain Monte Carlo method to fit the statistic to a galactic model including a thin disk, thick disk, and halo component. They derived a scale height of  $290_{-19}^{+20}$  pc and a central number density of  $0.29_{-0.13}^{+0.20} \text{ pc}^{-3}$ , with no correlation of model parameters with M-dwarf subtype, and consistent with previous studies. However, these studies do not probe statistics for later types. Recent work by [Sorahana et al. \(2018\)](#) found 3665 L dwarfs brighter than  $z=24$  by searching 130 square degrees of the Hyper Suprime-Cam Subaru Strategic Program data and found an average L-dwarf scale height of 340–420 pc. [Carnero](#)

Rosell et al. (2019) compiled a list of 11,745 photometrically classified L0-T9 dwarfs distances up to  $\sim 400$  pc by searching  $\sim 2,400$  deg $^2$  of the Dark Energy Survey (DES) data at a limiting magnitude of  $z=22$ . They estimated a large scale height of  $\sim 450$  pc. These last two studies provide another constraint on the number density of L dwarfs in the Galaxy using large samples ( $N > 10^3$ ); however, as in many imaging surveys, poor accuracy in spectral types significantly affects the derived parameters. Ultimately, the large uncertainties on spectral types of UCDs in imaging surveys poorly constrain their distances, and deep spectroscopic follow-up of these sources is not a priority for precious HST time.

A parallel approach is to use deep pencil beam samples of spectra in red optical and near infrared (NIR) with no prior selection of source type. NIR spectroscopy, in particular, samples the peak of UCD spectral energy distributions and measure broad molecular features that guide UCD classification schemes (Kirkpatrick 2005). Pirzkal et al. (2005) identified 18 late M and 2 L dwarfs in the Hubble Ultra Deep Field (HUDF) and estimated their spectral types by fitting templates from Kirkpatrick et al. (2000) to their Gradient-Assisted Photon Echo Spectroscopy (GRAPES, ref) taken with the xxx instrument (ref). This study inferred a disk scale height of  $400 \pm 100$  pc for M and L dwarfs. Another study by Pirzkal et al. (2009) used deep Advanced Camera for Surveys (ACS) slitless grism observations of the Probing Evolution And Reionization Spectroscopically (PEARS) fields (as part the Great Observatories Origins Deep Survey (GOODS) fields, Giavalisco et al. 2004) down to a  $z=25$  and spectroscopically identified 43 M4-M9 dwarfs. Using a thick and thin disk model, the study estimated a scale height for the thin disk of  $\sim 370$  pc, and  $\sim 100$  pc for the thick disk, a halo fraction between 0.00025–0.0005 consistent with previous estimates.

Masters et al. 2012 discovered 3 late T dwarfs the WFC3 infrared Spectroscopic Survey (WISPS) fields (Atek et al. 2010) identified by their strong CH<sub>4</sub> and H<sub>2</sub>O absorption features. The sample size was not large enough to put meaningful constraints on the scale height or the luminosity function L and T dwarfs beyond the local volume. In this paper, we expand upon this study by developing an effective method to select UCDs in similar surveys.

Section 2 describes the data, section 3 describes the selection process, section 4 discusses the result compared to a Monte-Carlo simulation

## 2. DATA

We obtained data from two surveys: the WFC3 Infrared Spectroscopic Parallel Survey (WISPS, Atek et al. 2010) and 3D-HST ( Momcheva et al. 2016, Brammer et al. 2012a, Skelton et al. 2014). These two surveys used the IR channel of the WFC3 camera (Kimble et al. 2008) providing low-resolution G102 ( $\lambda = 0.8\text{--}1.17 \mu\text{m}$ ,  $R \sim 210$ ) and G141 ( $\lambda = 1.11\text{--}1.67 \mu\text{m}$ ,  $R \sim 130$ ) grism spectra. Removal of the slit mask allows for the overlapping spectra of the  $136 \times 123$  arcsec inner FOV of the WFC3 camera. Figure ?? shows an WCF3 exposure of one of fields in WISP.

### 2.1. 3D-HST survey data

3D-HST a parallel survey of 248-orbits spanning  $\sim 600$  arcmin $^2$  as part of Hubble Cycles 18 & 19. This survey targets four standard deep extra-galactic fields: The All-wavelength Extended Groth Strip International Survey (AEGIS, Davis et al. 2007 ), Cosmic Evolution Survey (COSMOS, Scoville et al. 2007), Ultra-Deep Survey(UKIDSS-UDS, Lawrence & Others 2007), the Great Observatories Origins Deep Survey (GOODS-South and GOODS-North, Giavalisco et al. 2004), using the ACS/G800L and WFC3/G141 grisms in parallel. The goal of 3D-HST is to obtain as the the Cosmic Assembly Near-infrared Deep Extragalactic Legacy Survey(CANDELS survey, Grogin et al. 2011, Koekemoer et al. 2011. However, 3D-HST is only 70% of the total footprint of the CANDELS. Photometric catalog data products are described in Skelton et al. (2014) and combined data products in Momcheva et al. (2016)

The pointings for 3D-HST are designed to cover CANDELS area, therefore there are additional ground-based and space-based photometry from various other surveys in several optical and infrared filters. Each pointing in 3D-HST is observed by two orbits using the G141 grism and the F140W filter with typical exposure times of 5000 s for G141 AND 800 s for F140W. Observations for most of the pointings in the survey were conducted from October 2010 to November 2012. However, the GOODS-North field is a part of the A Grism H-Alpha SpecTroscopic survey (AGHAST, GO-11600;

PI: Wiener) and was observed between sept 16 2009 and sept 26 2010 and re-observed on April 19 and 24 2011, due artifacts and background issue, with exposure times of 800 s for F140W AND 5200S in G141.

Data reduction in 3D-HST involves reducing the both the direct F140W images and G141 grism images. The full description of the image reduction pipeline is described by Brammer et al. (2012b), Skelton et al. (2014) and Momcheva et al. (2016). Raw images were downloaded and passed through a pipeline that consists of removing satellite trails and artifacts through visual inspection, background -subtraction and flat-fielding. The main physical sources of time-dependent background are zodiacal continuum, scattered light and persistence from He emission at 1.083 micron. Both the reduction of the F140W and G141 images involved combining at most four dithered images. A standard method uses a drizzling algorithm implemented by the AXe software (Kuntschner et al. 2013; Kümmel et al. 2009). However, drizzling is designed to work well for a large number of images. The shortcomings of this method include the introduction of correlated noise between adjacent pixels. To avoid these issues, 3D-HST stacked all the dithered images onto one grid, given that the dithered images are all separated by the same number of pixels by the design of the survey. In addition, reducing the grism images require a reference image (different from the obtained F140W direct image) to generate a contamination global model of each pointing, to separate overlapping spectra and orders. The reference image was obtained by coming F125W, F140W AND F160W images of that pointing obtained from Skelton et al. (2014) data products, where the magnitudes of all objects in the fields are scaled to the F140W zero-point, and errors properly propagated. Based on the morphology and the magnitude of each source in the reference image, the full 2D-spectrum of each object was modeled from a 1D SED. This contamination model was then used to correct for overlapping spectra and orders. These 2D-spectra of exactly 312 pixels each are then extracted. The reference image and the direct images are on the same grid, therefore no source matching was required for source identification.

We used data products described by Momcheva et al. (2016) and the photometric catalog of sources in Skelton et al. (2014) retrieved from the survey’s website <sup>1</sup>. The extracted 1D spectra in 3D-HST survey are not continuum-corrected as shown in Figure 6. We obtained a correct continuum of each 3D-SHT spectrum by dividing the flux of the spectrum and the sensitivity curve of the detector provided in the data. We did not perform any additional reduction to the data.

## 2.2. *WISP survey data*

The WISP survey is a 1000-orbit HST pure-parallel survey covering 390 fields ( $\sim 1500 \text{ arcmin}^2$ ) that follows observing programs accepted on the Cosmic Origins Spectrograph (COS) and Space Telescope Imaging Spectrograph (STIS). The survey’s observing strategy as well as data-reduction is described in Atek et al. (2010). The goal of WISPS is to conduct a census of star-forming high-redshift galaxies. The fields in WISPS were chosen away from the galactic plane and 5.5 and 4.75 arcmin away from the fields of COS and STSIS. Given the pure-parallel nature of this survey, the fields are observed in G102, G141 grism with no dithering between exposure. Reference images were also taken using F110W (corresponding to G102) and F140W (corresponding to G141) imaging cameras. To reach the same depth in both G102 and G141, the ratio of exposure times was fixed at 2.4:1, while the exposure ratio of exposure times for imaging and grism is 6:1.

Data reduction and grism extraction was performed using a combination of **AXe** software (Kuntschner et al. 2013; Kümmel et al. 2009) and custom IDL pipelines to remove additional background and to flag bad pixels. The main sources of background are zodiacal light, and earth thermal emissions. Grisms spectra in WISPS have little crowding of the same fields given their high galactic latitudes, but multiple spectral orders do overlap. WISPS provides an estimate of contamination of each spectrum computed using **AXe** and source catalogs in WISPS were generated using SExtractor (Bertin & Arnouts 1996). We obtained WISPS G102 and G141 grism data as well as broad-band

<sup>1</sup> <https://3dhst.research.yale.edu/Home.html>

F110W, F140W, F160W photometric data and source catalogs from the Mukuliski Archive for Space Telescope (MAST<sup>[2](#)</sup> ).

### 3. SELECTION OF UCDS

#### 3.1. *Calibration Samples*

To find a sample of UCDS in WISPS & 3D-HST data, we created a calibration sample of known UCDS, with similar features, e.g spectral coverage and resolution to define our selection methods and quantity their efficiencies and biases. We obtained 2056 M7-T9 low-resolution ( $\sim$ 75-120), NIR (0.9-2.5  $\mu$ m) spectra of nearby brown dwarfs with median SNR  $>10$  from the SpeX Prism Library (SPL, Burgasser 2014a, <https://cass.ucsd.edu/~ajb/browndwarfs/spexprism/library.html>) of UCDS. We will refer to this sample as the templates/SpEX sample. In addition, we compiled a list other UCD spectra taken with the same instrument. We used the 77 UCDS from Manjavacas et al. (2018) observed with the WFC3 as part of a study of cloud properties of hot Jupiters and brown dwarf atmospheres and compilation of a WFC3 UCD library. The Schneider dataset is a list of 22 Y dwarfs obtained by Schneider et al. (2015) using the WFC3 camera with the same resolution and wavelength coverage. These objects were targeted as a part of a program to determine spectroscopic markers of the T/Y dwarf transition. We combined these three sets of spectra.

#### 3.2. *Pre-selection*

##### 3.2.1. *Point-source Cut*

We combined all grism data and photometry from both surveys and obtained a total of 271915 grisms that have corresponding photometry in the provided photometric catalogs. To narrow down our selection, point sources were identified using `Source Extractor`'s stellarity index `CLASS_STAR`  $\neq 0$ . 3D-HST provides an additional `star_flag` flag for point-sources based on their F160W magnitudes and the flag `FLUX_RADIUS`, but we find that this flag eliminates 3 UCDS from 3D-HST in the selected

<sup>2</sup> <https://archive.stsci.edu/prepds/wisp/>

sample of UCDs, hence the flag was ignored. We reduced the sample down to 110930 spectra, that is 40.7% of the total number of spectra.

### 3.2.2. *J-band SNR rejection*

UCDs display a strong H<sub>2</sub>O and CH<sub>4</sub> absorption features in the J and H bands. We do not expect other objects in this survey to display similar molecular broad features, hence to narrow down our selection, we defined a signal-to-noise ratio in the J-band continuum (hereafter J-SNR) in the wavelength region of  $1.2 \mu\text{m} \leq \lambda \leq 1.3 \mu\text{m}$ . This J-SNR captures the amount of flux in the J-band, hence we eliminated the lowest SNR objects by making a cut at J-SNR= 3 retaining 46370 spectra/grisms, that is 38.7 % of the original point-source sample and 15.8% of the total number of spectra. We also measured the J-SNR for all the spectra in our calibration samples in a similar fashion.

### 3.3. *Spectral Fitting and F-test*

After the J-SNR cut, we fitted spectra to UCDs SpeX spectra of spectral standards using a  $\chi^2$  minimization method, following the method of Kirkpatrick et al. (2010). We obtained a spectral type classification all available WISP and 3D-HST spectra. We also compared every spectrum to a straight line in the same wavelength region and measured  $\chi^2$ . These two fits help distinguish between spectra that could potentially have absorption features in this region, and spectra that have no interesting features and/or noisy spectra in this wavelength region. The  $\chi^2$  of a line ( $\chi_L^2$ ) or a standard ( $\chi_T^2$ ) is given by

$$\chi_L^2 = \sum_{\lambda=1.15\mu\text{m}}^{1.65\mu\text{m}} \frac{(a + b\lambda - \text{Sp})^2}{\sigma^2} \quad (1)$$

$$\chi_T^2 = \sum_{\lambda=1.15\mu\text{m}}^{1.65\mu\text{m}} \frac{(\text{Sp} - \alpha T)^2}{\sigma^2} \quad (2)$$

$\alpha$  is scale-factor defined as

$$\alpha = \sum_{\lambda=1.15\mu\text{m}}^{1.65\mu\text{m}} \frac{(\text{Sp} - \alpha T)^2}{\frac{T^2}{\sigma^2}} \quad (3)$$

$\text{Sp}(\lambda)$  is a WISP or 3D-HST spectrum and  $\sigma^2$  is the noise in the WISP or 3D-HST spectrum a and b are the parameters of the best-fit line from least-squares and T is the template.

We then use an F-test as a statistical hypothesis testing static to separate noisy/linear spectra from the rest of the sample implemented by Scipy [Jones et al. 2001](#)– as `scipy.stats.f.cdf`. A flat spectrum is defined as having  $F(\chi_s^2/\chi_l^2) < 0.4$  meaning that the probability of the standard being a better fit to the spectrum than a line is <than 40%. This cut yields only 8148 objects, that is 18.9% of point-sources with  $J\text{-SNR} > 3$ , 7.3% of all point-sources and 3% of the original number of spectra we obtained from both surveys. These three steps eliminated most of the noisy contaminants.

### 3.4. Spectral Indices

After eliminating noisy and possible extra-galactic contaminants, we narrowed down the selection to true UCDs. UCDs display strong CH<sub>4</sub> and H<sub>2</sub>O molecular features in  $1.1 \mu\text{m} < \lambda < 1.7 \mu\text{m}$  region ([Burgasser 2001](#)), they can be separated from other stellar/galaxy populations using these features. Spectral Indices have traditionally been used to determine spectral types ([Tokunaga & Kobayashi 1999](#), [Cushing et al. 2000](#), [Allers et al. 2007](#), [Burgasser et al. 2007](#)). Thus, we defined spectral indices in five wavelength bands: 1.15–1.20  $\mu\text{m}$ , 1.246–1.295  $\mu\text{m}$ , 1.38–1.43  $\mu\text{m}$ , 1.56–1.61  $\mu\text{m}$ , or 1.62–1.67  $\mu\text{m}$ ; denoted by H<sub>2</sub>O-1, J-Cont, H<sub>2</sub>O-1, H-Cont, and CH<sub>4</sub> respectively. Each index is the ratio of the median flux in these bands and the uncertainties for each index are estimated by random sampling, assuming these uncertainties are Gaussian-distributed. The index is given by

$$\text{Index} = \frac{\langle F(\lambda_1 < \lambda < \lambda_2) \rangle}{\langle F(\lambda_1 < \lambda < \lambda_2) \rangle} \quad (4)$$

, where at each wavelength i, we draw fluxes normally distributed according to the noise in the spectrum:

$$\{F(\lambda_i)\} \sim \text{Normal}(\langle F(\lambda_i) \rangle, \sigma(\lambda_i)) \quad (5)$$

.  $\sigma(\lambda_i)$ ) is the noise at that wavelength, and  $\langle F(\lambda_i) \rangle$  is the flux at that wavelength.

We defined selection criteria using boxes/parallelograms in each of 45 independent, index-spectral index spaces. We expect UCDs with similar spectral types to cluster or follow a linear trend, away from the contaminants while the evolution of the relative strength H<sub>2</sub>O and CH<sub>4</sub> bands with subtype

should distinguish classes. We chose the following subtypes given their similarities : M7-L0, L0-L5, L5-L0, T0-T5, T5-T9, Y dwarfs and subdwarfs, however, these distinction need not be as rigid.

To define the parameters of each selection criterion/box, we fitted a characteristic line to each index pair (x-index, y-index) within a subtype, defining the slope/direction of the box:  $y = m \times x\text{-index} + b$ . Each box has four vertices ( $v_1, v_2, v_3, v_4$ ) computed as  $(x_{\max}, x_{\min}) = \text{median}(x\text{-index}) \pm 3 \times \text{std}(x\text{-index})$ . On the x-axis, if  $x_{\max}$  is greater than the maximum of x-index, or if  $x_{\min}$  is less than the minimum of the x-index, i.e the box extends beyond the subtype, we set  $x_{\min}$  and  $x_{\max}$  and the minimum and maximum of x-index respectively. The extent of the boxes on the y-axis are determined by  $(y_{\max}, y_{\min}) = m \times (x_{\max}, x_{\min}) + b \pm 0.4 \times dy$ , where  $dy$  is the range of y-index ( $\text{max}(y\text{-index}) - \text{min}(y\text{-index})$ ). From these values, we define  $v_1 = (x_{\min}, y_{\max})$ ,  $v_2 = (x_{\min}, y_{\min})$ ,  $v_3 = (x_{\max}, y_{\max})$ ,  $v_4 = (x_{\max}, y_{\min})$ . These boxes are designed to enclose most of the objects in each subtype and to avoid outliers. We used rectangular boxes, for their simplicity, and low-contaminations for subtypes M7-L0, L0-L5, L5-T0, and Y dwarfs, where the vertices were determined in the same manner but with  $m=0$  and  $b = \text{median}(y\text{-index})$ .

To assess the effectiveness of this method, we defined a completeness and a contamination statistic for each of the subtype group as follows:

$$CP = \frac{TEMP_s}{TEMP_{tot}} \quad (6)$$

$$CT = \frac{WFC3_s}{WFC3_{tot}} \quad (7)$$

where  $TEMP_s$  is the number of templates selected by the box,  $TEMP_{tot}$  is the total number of SpeX templates,  $WFC3_s$  is the number of WISPS and/or 3D-HST spectra selected by the box,  $WFC3_{tot} = 8148$  is the total of spectra. We only employed criteria with the lowest contamination and highest completeness to select UCDs. The best criteria for each of the subtype groupings are those with less than 1% contamination (except for subdwarfs) and with >90% completeness; they are summarized in Table 1.

As a naming convention, each criteria is named by the ratio of indices on the x-axis and the ratio of fluxes on the y-axis. The best selection criteria are the following for each subtype are: H<sub>2</sub>O-1/J-Cont H<sub>2</sub>O-2/H<sub>2</sub>O-1 for the subtype of L0-L5 sensitive to the H<sub>2</sub>O absorption feature in the J-band; H<sub>2</sub>O-1/J-Cont CH<sub>4</sub>/H-Cont for the L5-T0 sampling the relative ratio of H<sub>2</sub>O and CH<sub>4</sub> features; H<sub>2</sub>O-1/J-Cont CH<sub>4</sub>/H<sub>2</sub>O-1 for the M7-L0 subtypes, sensitive to the H<sub>2</sub>O in the J-band and CH<sub>4</sub> features; H<sub>2</sub>O-2/J-Cont CH<sub>4</sub>/H-Cont for the T0-T5 subtypes, sensitive to the H<sub>2</sub>O and CH<sub>4</sub> in the H-band; H-cont/H<sub>2</sub>O-1 CH<sub>4</sub>/J-Cont for the T5-T9 subtypes, sensitive to H<sub>2</sub>O and CH<sub>4</sub>. We use the index CH<sub>4</sub>/H<sub>2</sub>O-1 H<sub>2</sub>O-2/J-Cont to select Y dwarfs from the Schneider sample and H<sub>2</sub>O-1/J-Cont CH<sub>4</sub>/J-Cont for the subdwarfs in the SpeX sample. In total, we selected 2910 spectra out of 8148. The large number comes from high contaminations for the M7-L0 and subdwarf boxes.

As a final step, after all selection has been applied, we visually inspected all the candidates UCDs to confirm their spectral type, and to remove missed outliers. We estimated the false positive rates for our methods after visual inspection and characterization of the UCDS. The false positive rate (FP) is given by

$$FP = 1 - \frac{WFC3_{true}}{WFC3_s} \quad (8)$$

where WFC3<sub>true</sub> is the total number of objects that are in the spectral type range, and that are true UCDs. Our best selection criteria have FPs >90% which is to be expected given the number of true UCDs is much smaller than the number of spectra. Nevertheless, the number of spectra targeted for visual contamination have been down-selected from more than 200000 to  $\sim 3000$ .

### 3.5. Random Forest Classifier

As an alternative to using selection boxes in 2D-space, we trained a random forest classifier by deploying `RandomForestClassifier` implementation by `scikit-learn` (Pedregosa et al. 2012) to classify potential UCDs in both surveys. Random forests have been shown to reliably predict M-dwarf subtypes based on colors (Hardegree-Ullman et al. 2019) analogous to spectral indices. In addition, random forests have been proven to perform star-galaxy classification in transient surveys, using photometry alone (Miller et al. 2017). Random forest algorithms use a set of independent

decision trees constructed based on a random set of features, they assign a final label by averaging the classifications obtained by each decision tree. Furthermore, random forests are a reliable method used to obtain classification for large datasets, given that the algorithm is relatively fast, unbiased by noisy features and easy to implement.

The training set of 11019 objects is composed of 8283 visually confirmed non-UCDs from several iteration of the box-selection method in the previous section, 77 objects from the Manjavacas set, 22 objects form the Schneider set. We labeled these sources using two labels: UCDs, which are objects with spectral types  $\geq M7$ , and non-UCDs which are objects with spectral types  $\leq M7$  and/or part of the visually confirmed as non-UCDs. his labeling results in 2148 objects labeled as UCDs (label=1) 8871 and with label=0.

Choosing an appropriate set of features is an important part of designing a good machine learning classifier. By intuition, spectral indices, although they are correlated, are a good set of features to use. We added the signal-to-noise ratio in the J-continuum, the two  $\chi^2$ s and their ratio, and the F-test value as additional features. For missing features, we replaced those values with -99999.9 and scaled all features in the range [0, 1] using `MinMaxScaler`. To test the accuracy of our classifier, we use a procedure similar to that of ([Miller et al. 2017](#)). We used 2-fold cross validation score and split the training by 50% and 50% partitions. We computed the accuracy by starting with one index as a feature and then adding additional features. We tracked the accuracy of the classification using cross-validation (CV) scores for each additional feature. With only one spectral index, we achieved a classification score of 75.4%, with all additional features we achieved a CV score of 98.68 %. We deployed the classifier on the 110930 point-source objects in both surveys with  $J\text{-SNR} > 3$ , classifying 490 sources as UCDs, among which 109 are real UCDs ( M7-T9). The false positive rate (FP) for this method, using the same definition is 77.7%.

### 3.6. *Sample Characterization*

#### 3.6.1. *M dwarfs*

We found 121 objects with spectral types of M7-M9, these objects are defined by the H<sub>2</sub>O absorption features at distances between 500 pc and 4 kpc. We show the distance distribution of all the UCDs in the sample in Figure (insert fig ). While T dwarfs are limited in the nearby  $\sim 500$  pc, M and L dwarfs are observed up to  $\sim 3$ kpc; this includes sources outside our effective limiting magnitude. The observed galactic distribution of the UCDs is consistent with the galactic distribution and depths of the pointings in the survey. The farthest L dwarf is at xxx and the farthest T dwarf is xx at 2000 pc . This sample include 3 T dwarfs identified by Masters et al. (2012) including perhaps the farthest spectroscopically-identified T dwarf to known. We report the magnitude distribution of our sample in fig xx and table xx. The faintest objects in the sample have magnitudes of F110W=24.3, F140W=25.2, F160W=25.2.

### 3.6.2. Robust L & T dwarfs

*WISP L dwarfs*—We identified x early (L0-L5) L dwarfs in WISP. WISP 0927+6027 is an L0 dwarf at  $\sim 320$  pc discovered in the Par21 pointing of the WISPS survey. It has an apparent magnitude of F140W=18.6 and fits to the L0 dwarf standard with good agreement except for the wavelength ranges of 1.35 to 1.5  $\mu$ m and 1.65 to 1.7  $\mu$ m due to a possible underestimation or overcorrection of the contamination in those wavelength regions. WISP 1429+3224 is classified as an L0 at  $\sim 1.5$  kpc discovered in the Par378 pointing of the WISP survey. Its apparent magnitude is F140W=22.4 and it has a low SNR (J-SNR=8). Major H<sub>2</sub>O strength defining that spectral class are present in the spectrum despite the the rise in noise in certain parts of the spectrum. The apparently visual companion is not a UCD, and was not selected by our methods. WISP 1605+1447 is an L0 dwarf at  $\sim 1.5$  kpc found in the Par240 field of the WISP survey. The fit to the standard is relatively poor, and there is a ramp-up of signal  $\lambda 1.6 \mu\text{m}$ , a typical feature in WISP spectra due to a less-precise estimation of the background. WISP 1004+5258 is an L1 dwarf at  $\sim 1.8$  kpc found in the Par438 field/pointing of the WISP survey. There is a puzzling extra flux at 1.3 micron. This object might not be a UCD. WISP 0246-0104 is an L1 dwarf at  $\sim 1.5$  kpc in the Par438 pointing of WISPS. It is a noisier spectrum, but with major features offering a good fit to the standard. WISP 1150-2033 is classified as L1 at  $\sim 380$  pc. It is a bright detection (F160W= 19.2) with a high SNR (J-SNR = 57).

It's a good fit to the standard. WISP 0015-7955 is classified as L1  $\sim 1.5$  kpc in the Par244 pointing. It is a faint source with a J-SNR of 6 and F140W=22.2 but a relatively good fit to the standard. WISP 1618+3340 is another bright L dwarf in WISPS. It has an apparent magnitude of F110W =21.7 putting it at a distance of  $\sim 1$ kpc. WISP 1133+0328 an L1 at  $\sim 1$  kpc with F140W=22.0 with no particular interesting features. WISP 1154+1941 is an L1  $\sim 1$  kpc in a Par338. The spectrum shows a ramp-up in flux at longer wavelength, a common feature in WISP data.

WISP 1124+4202 is the only late L dwarf in WISPS. Its G141 spectrum with J-SNR =11 is in a good agreement with the SpeX spectral standard. The object has an F160W=21.5 and an estimated distance of  $\sim 650$  pc.

*3D-HST L dwarfs*—For early dwarfs, L1 GOODSS 0333-2751, a bright detection at  $\sim 1.1$  kpc with a brightness of F140W=21.4 and a J-SNR of 34. The G141 spectrum fits well to the standard except for the region  $\lambda \in [1.3, 1.4] \mu\text{m}$ . However, there is no visible contamination in the spectrum at that specific region, the poor fit might be attributed to the telluric correction. UDS 0217-0509 is an L1 dwarf in UDS-25, a nearly perfect fit to the standard. GOODSN 1236+6211 is an L2 dwarf in GOODSN-33 with a J-SNR of 12. The object is in close angular separation with other extra galactic contaminants, but the its spectrum has very little contamination. GOODSN 1236+6209 is a low-SNR detection (J-SNR = 5) classified as L2 at  $\sim 4$  kpc in the GOODSN-34 pointing. This object is the farthest early L dwarf in the sample.

*WISP T dwarfs*—There are only x early T dwarfs from WISPS in the sample. WISP 1003+2854 is classified as T0 at  $\sim 1$  kpc. The G141 spectrum displays deep H<sub>2</sub>O and CH<sub>4</sub> features with a J-SNR of 6. The spectrum is a poor fit to the standard in noisy regions. The object has a magnitude of F160W=23.1 placing it at  $\sim 1$  kpc. WISP 0437-1106 is another robust identification, classified as T3 and with an apparent magnitude of F110W=24.3 found in the Par463 pointing of WISP. The J-SNR of the spectrum is 4, and the estimated distance is  $\sim 800$  pc.

In terms of mid-to late T dwarfs, we found 3 objects previously discovered by [Masters et al. \(2012\)](#). WISP0307-7243 is classified as T4 at  $\sim 500$  pc, WISP1232-0033 is classified as T7 at  $\sim 200$  pc and

WISP1305-2538 is classified as T9 at  $\sim$ 300 pc. Our classifications and distances agree with the previous classification

*3D-HST T dwarfs*—We find one early T dwarf is COSMOS-23: COSMOS1000+0217 is classified as T3 at  $\sim$ 900 pc, with an apparent magnitude of F140W=23.8. The estimated J-SNR of this its G141 spectrum is 5, and the spectrum is a robust fit to the standard. However, given the crowded field, the image is difficult to identify. We found another T dwarf in AEGIS-03, AEGIS1418+5242 is classified as T4, with a high SNR (J-SNR=21) and apparent magnitude of F140W=22.7 implying a distance of  $\sim$ 500 pc. The spectrum is a good fit to the spectral standard and there is no visible contamination by nearby objects in the field or other spectral orders. Finally, we detected 2 T dwarfs in the GOODS fields: GOODSS0332-2741 is classified as T6 with a J-SNR=31 and F140W=22.1 placing it at a distance of  $\sim$ 300 pc. GOODSS0332-2749 is classified as a T3 with a J-SNR of 13 at  $\sim$ 500 pc. Both spectra are good fits to the spectral standards.

### 3.6.3. Subdwarfs, Y dwarfs & Binaries

[WORKING ON THIS SUBSECTION] We searched for subdwarfs and Y dwarfs by creating selection criteria for these subtypes. However, we did not find any obvious subdwarfs or binaries in the sample with the two methods. This is unsurprising given that estimates of the ratio of subdwarfs to dwarfs is 1/400 (ref) and the binary fraction of UCDs is very low  $< 10\%$ .

### 3.6.4. Borderline L & T dwarfs

T

### 3.6.5. Absolute Magnitude Spectral Type Relations

We create an absolute magnitude-spectral type relation to estimate distances of objects in our observed sample. These relations are built from the relations of Dupuy & Liu (2012). We first computed an offset/color between 2MASS J and H magnitudes and AB Hubble magnitudes by convolving the SpeX standard for a given spectral type with the respective filter. This offset in convolutions is then added to the absolute magnitude-spectral type relations in 2MASS J, H filters

to obtain the new relation in Hubble filters. Error propagation is done using Monte-Carlo sampling, we report these relations in Table 3 and show them in Figure 9

## 4. PROBING GALACTIC STRUCTURE

### 4.0.1. *Limiting Magnitudes*

We aim to constrain the number density of UCDs; an accurate estimate of the effective distance/volume of each pointing is crucial. Momcheva et al. 2016 reported the effective depths of all the pointings in 3D-HST, however, given the SNR cut, we expect the a brighter limit than these reported depths. Hence, we adopted the faintness limits of F110W=22.0, F140W=21.5, F160W=21.5 for WISP fields, and F140W=22.5, F160W=22.5 for 3D-HST fields. For the bright end, we used the bright limits of F110W=18.0, F140W=16.0, F160W=16.0 for WISPS fields and F140W=16.0, F160W=16.0 for 3D-HST fields following the peak of the distribution of magnitudes (Figure 11) for all the point sources satisfying the SNR cut. These bright limits correspond to limiting distances hence effective volumes for each spectral type, using the absolute magnitude spectral type relation defined in this work.

### 4.1. *Monte-Carlo Simulation*

The observed number of UCDs as a function of spectral type depends on the local luminosity function, the probed effective volume, and selection biases. We construct a Monte-Carlo simulation to fully estimate these effects following methods from Reid et al. (1999) and Burgasser (2004). All these steps are illustrated in the graphical model in Figure ?? and explained in this section.

#### 4.1.1. *Local Luminosity Function*

The local luminosity function ( $\Phi[mag^{-1}pc^{-3}]$ ) of UCDs have been measured using various methods. However, this sample of UCD is distant ( $\sim kpc$ ), therefore, to avoid any biases, we simulate a "semi-empirical" luminosity function using two fundamental stellar distributions: the mass function and the age distribution as follows:

- **Mass (M),  $N_0 \leftarrow \alpha$**  : we draw a sample of  $2 \times 10^5$  objects from a power-law mass function parametrized by  $\alpha$  for a range of masses between  $0.001 M_\odot$  and  $0.15 M_\odot$ .

$$P(M) = \frac{dN}{dM} \sim \left( \frac{M}{M_\odot} \right)^{-0.6} \quad (9)$$

. We define a normalization factor ( $N_0$ ) given by

$$N_0 = 0.005 M_\odot^{-1} pc^{-3} \sum_{M \in [0.01 M_\odot, 0.09 M_\odot]} M \cdot P(M) \quad (10)$$

as the number density of objects in this simulated sample with masses between 0.01 and 0.9 in our simulation([Reid et al. 1999](#), [Chabrier 2001](#)). For this part of the simulation, the samples of masses were generated by inverting the cumulative distribution (CDF) and using a random number generator to obtain the corresponding values. The CDF ( $m$ ) for a given mass  $m$  is given by

$$CDF(m) = \frac{1}{C} \int_{M=0.001}^{M=m} P(M) dM = \frac{1}{C} \int_{M=0.001}^{M=m} M^{-0.6} dM \quad (11)$$

, where  $C$  is the normalization constant (i.e CDF for  $m=0.15$ ). With this mapping, one can obtain different values of the of  $m$  by choosing random number  $x$  ( $x=CDF$ )  $\in [0, 1.]$ .

- **Age  $\sim$  uniform** : we assigned each of these UCDs an age drawn from a uniform uniform age distribution spanning 100 Myr–10 Gyr. Although there are different parametrization of the star-formation history of the Galaxy, this age distribution correlates with the observed scale heights and velocity distribution of the UCD populations ([Ryan et al. 2017](#); [Rujopakarn et al. 2010](#); [Aumer & Binney 2009](#)). We then keep the age uniform and vary the scale heights, given that varying the scale height is a simpler parametrization.
- **$T_{eff} \leftarrow \text{SpT} \leftarrow (\text{Mass}, \text{Age})$**  : we assigned a temperature to each of the simulated objects, using a linear interpolation evolutionary model grids from [Baraffe et al. \(2003\)](#). We then converted temperatures to a spectral types (M7-T8) using the polynomial relation from [Filippazzo et al. \(2015\)](#). This resulting distribution of spectral types will then be used to estimate our selection biases.

#### 4.1.2. Effective Volumes

The observed effective volume of each pointing depends on the scale height and the limiting magnitude of the survey. We compute these volumes using the following steps:

- The limiting magnitudes for both 3D-HST and WISPS are defined visually as the peak of the magnitude histogram as shown in Figure 11 and explained in section ???. These magnitudes provide the distance limits for a given spectral type and pointing  $d_{max,min}$  determined by

$$\log d_{min,max} = \frac{1}{5}(m - M(SpT)) + 1 \quad (12)$$

where  $m$  is the faint or the bright limit of the survey and  $M(SpT)$  is the absolute magnitude for that spectral type. For pointings in 3D-HST, we use F140W magnitudes and for WISP pointings we use F110W magnitudes. Absolute magnitude calculations are described in section ???. A complete treatment would account for the effect of dust extinction, however, the pointings in 3D-HST and WISPS are located away from the galactic plane to avoid this problem.

- We adopt a 1-component galactic disk model parametrized by  $\theta = (h, l)$  where  $h$  and  $l$  are the scale height and the scale length of a given stellar population. Using Burgasser (2004), the spatial density of stars in given direction  $\vec{p}$  and distance ( $d$ ) by

$$\rho(\vec{p}, d) = \rho(r, z) = \rho_0 \cdot \operatorname{sech}^2\left(\frac{|z - Z_\odot|}{2h}\right) \cdot \exp\left(-\frac{R - R_\odot}{l}\right) \quad (13)$$

.  $L$  is fixed at 2600 pc while  $h$  is varied from values of 100 pc, 250 pc, 275 pc, 300 pc, 325 pc, 350 pc and 1000 pc drawn from possible values of scale heights predicted from cooling evolutionary models of UCDS (Ryan et al. 2017).  $R_\odot$  and  $Z_\odot$  are the sun's position from the galactic center, fixed at 8300 pc and 27 pc respectively. The change from  $\rho(\vec{p}, d)$  to  $\rho(r, z)$  involves a coordinate transformation from sky to Galactic coordinates.

- $\mathbf{V}_c \leftarrow \theta = (\mathbf{h}, \mathbf{l})$  and  $\mathbf{V}_{eff} \leftarrow (\mathbf{d}_{max}, \mathbf{d}_{min}, \mathbf{V}_c)$ : given the Galactic structure model, we compute a volume correction ( $V_c$ ) up to distance  $d$ , in a given direction  $\vec{p}$ . This term is the ratio of exponential density to a uniform space density in a given direction.

$$V_c = \frac{\int_0^d \rho(x, \vec{p}) \cdot x^2 dx}{\int_0^x x^2 dx} \quad (14)$$

, where  $x$  is the 3D-distance in that line of sight. The effective volume of each pointing ( $\vec{p}$ ) and spectral type is

$$V_{eff}(\vec{p}) = V_c(d_{max} - d_{min}, \vec{p}) \cdot (d_{max}^3 - d_{min}^3) \cdot \Delta\Omega \cdot \frac{1}{3} \quad (15)$$

. Where the  $\Delta\Omega$  is the solid angle of each pointing fixed at  $\Delta\Omega \approx 3.47 \times 10^{-7}$  radian<sup>2</sup> for each pointing.

#### 4.1.3. Selection Effects

Because we applied several selection criteria to narrow down our sample for visual confirmation, it is possible we may have missed a few UCDs in the WISPS/3D-HST fields; particularly low SNR or peculiar objects due, in part, to uncertainties in spectral indices. Hence, the observed volumes objects must be corrected by a factor proportional to our selection biases. To fully quantify these effects, we generated a distribution of low-resolution spectra uniformly sampling our SNR distribution across a wide range of SNRs and measured their recovery rate through this selection process by augmenting the SpeX sample to cover 3 orders of magnitude in SNR. To create this sample, we picked the top 20 highest SNR spectra with a median SNR between 50 and 200 L0-T9 objects in the SpeX sample, we added Gaussian noise each spectrum for an iteration of  $10^3$  steps creating a new sample of 21800 spectra. Each new "degraded" spectrum is created as

$$\{F(\lambda_i)\} \sim \text{Normal}(< F(\lambda_i) >, \sigma^t(\lambda_i)) \quad (16)$$

.  $\sigma^t(\lambda_i)$  is the target noise at a wavelength  $\lambda_i$ , and  $< F(\lambda_i) >$  is the flux of the original spectrum at that wavelength. We computed all relevant statistics for each of the degraded spectra, including J-SNR, spectral indices, F-test, and the two  $\chi^2$ s. We applied our selection processes to this sample of simulated spectra by measuring spectral indices and applying first F-test criterion where F-test  $< 0.4$ , box index-index selection criteria and the random forest classifier.

In addition, after degrading the spectrum, the object will change its original classification. We defined a selection probability that accounts for the number of objects falling outside our classification range (M7-Y0) after degradation and the selection process itself in a given signal-to-noise range ( $\Delta$

J-SNR bin of 2.0). We denote this probability of selection of  $\mathcal{S}$ (J-SNR, SpT)

$$\mathcal{S}(\text{J-SNR}_i, \text{SpT}) = \frac{N_{s,i} + N_{m,i}}{N_{tot,i}} \quad (17)$$

where  $N_s$  is the number selected spectral type and SNR bin, and  $N_{tot}$  is the total number of objects in that bin. Where  $N_{s,i}$  is the number of objects in a bin i, selected by our selection process and  $N_{m,i}$  is the number of objects in a bin i that fall outside the spectral type range of M7-Y2 after degradation.  $N_{tot,i}$  is the total number of spectra in that signal-to-noise ration bin. These selection probabilities are showcased in Figure x.

For each simulated spectral type from the mass function (section 4.1.1), we computed a selection probability  $\mathcal{S}$  parametrized by the expected signal-to-noise ratio (J-SNR) and spectral type (SpT) using the following steps:

- $\mathbf{d} \leftarrow (\theta=(\mathbf{h}, \mathbf{l}), \mathbf{d}_{max}, \mathbf{d}_{min})$ : we assign a distance to each of drawn from the Galactic structure model. The likelihood of distance (d) given a spectral type (SpT) pointing  $\vec{p}$

$$P(d|\vec{p}) \sim \rho(d, \vec{p}) \cdot d^2 \quad (18)$$

. We then assign each object a randomly drawn distance from all the 533 pointings/directions in both surveys. For a given spectral type the distance is limited to  $d_{min}/2 < d < 10 \times d_{max}$  to account for objects scattered in the observed volume. Samples for this part of the simulation were generated using Pymc for a number of samples  $N=20000$ , sampling each scale height independently using a standard Metropolis-Hastings Algorithm.

- **J-SNR  $\leftarrow$  (F110W, F140W, F160W)  $\leftarrow$  (d, SpT)** : we estimate an observable signal-to-noise ratio of each object as observed by the WFC3 instrument based on the observed sample. We fit a second-degree polynomial to the observed magnitudes (F110W, F140W, F160W) and SNR-J of our observed sample. We then use our derived absolute-magnitude spectral type relations to estimate the apparent magnitude of each object in our simulated sample based on its randomly-assigned distance and spectral type. The apparent magnitude- J-SNR relation is then used to estimate a signal-to-noise ratio as observed with the WFC3 instrument.

- $\mathcal{S} \leftarrow (\text{J-SNR}, \text{SpT})$ : we assigned a selection probability, as previously defined, to every simulated object in the observed, that is an object with magnitude and signal-noise ratios within our cuts ( $\text{J-SNR} < 3$  and  $\text{F110W} > 22.5$  (the limiting magnitude from 3D-HST)).
- The expected number of expected objects per spectral type is then by a simple product of selection probabilities, effective volume scaled by the normalization factor.

$$N_{sim}(\text{SpT}) = N_0 \cdot V_{eff}(\text{SpT}) \cdot \sum_i \mathcal{S}(\text{J-SNR}_i, \text{SpT}) \quad (19)$$

. We compared these numbers to the observed numbers of UCDs for each age distribution in figure 13

#### 4.2. Results

The resulting spectral type distribution is consistent with expectations given atmospheric cooling effects (Burgasser 2004) from evolutionary models. As UCDs age, they quickly pile up on at the lower end of the spectral type distribution and cooler temperatures. The effective volume for each spectral type and scale heights span 6 orders of magnitude in  $pc^3$ , and given that earlier spectral types probe larger volumes, the effect of scale heights is more distinguishable for these types ( $\text{SpT} \leq T5$ ). The resulting distribution of distances is smooth, given the simplicity of our Galactic structure model. Ryan et al. (2017) estimated a change in scale height of ( $\Delta h \sim 50$  pc) in the mid-L dwarf regime by comparing galactic models for different cooling scenarios; while the scale height in for late M dwarf and L is consistent with our simulations, and despite the high accuracy in spectral types for the sample of UCDs presented in this study, the relatively small sample size of L& T dwarfs might not put meaningful constraints on the scale height variations. Nevertheless, the total number of observed M7-T8 dwarfs ( $136 \pm 11$ ) is consistent with a scale height between 325-350 pc.

We predict more T dwarfs observed, in part due to a possible underestimation of the observed volume given that limiting magnitudes were visually estimated [there has been a more empirical way of doing this, like KDEs]. Moreover, the L/T transition region is sensitive to unresolved binaries (Bardalez Gagliuffi et al. 2014). Burgasser (2007) shows that given a spectral binary fraction of  $\sim 10\%$ , the surface densities for volume-limited sample of primaries and combined systems are similar

but present a slight bump ( $\Delta\Sigma \lesssim 5 \times 10^{-5} \text{ deg}^{-2}$ ) for early T dwarfs. Given our total search area of  $\sim 0.6 \text{ deg}^2$ , we do not expect a significant effect of the spectral binary fraction to the reported densities, hence we assumed that none of the UCDs in this study are unresolved binaries in our simulation.

Metallicity effects affect the number of subdwarfs we expected in this sample. UCDs in the thick disk and the halo have similar kinematic ages with stellar populations in these parts of the Galaxy; and UCDs at different metallicities follow different evolutionary tracks. L subdwarfs in the local neighborhood are therefore rare, and this study does not significantly probe large volumes in the thick disk and halo. [Lodieu et al. \(2017\)](#) found  $0.04 \times \text{deg}^{-2}$  L subdwarfs in the UKIDSS/SDSS fields; in fact, we expect the number of subdwarfs to be  $\sim 400$  times lower than the expected number of dwarfs in the sample. Although the parallel fields in 3D-HST & WISP are deep, the total search area remains low, hence it is not surprising that we did not find any L subdwarfs in the sample.

## 5. SUMMARY

The WISPS & 3D-HST surveys provide NIR G141 (1.1-1.14  $\mu\text{m}$ ) spectroscopic data and broadband F140W, F110W & F160W photometry for thousands of galaxies and point-sources observed in parallel mode with other on-going HST surveys. We made a point-source cut using in the surveys and obtained 271915 point-sources. Using NIR spectral indices that sample the prominent H<sub>2</sub>O and CH<sub>4</sub> absorption features in UCD atmospheres, we created selection criteria based on a calibration sample of templates. We have presented two methods for selecting UCDs in deep HST surveys potentially applicable future infrared parallel surveys. Both methods rely on spectral indices defined to trace H<sub>2</sub>O and CH<sub>4</sub> features prominent in the NIR band of UCDS. The box selection method is efficient (completeness  $>90\%$ ) but with relatively high contamination rates that could be significantly reduced by eliminating the lowest SNR sources. This method is not effective for selecting very low SNR sources due to large scatter in indices and early M-dwarfs as the absorption features in these wavelength ranges are shallow. However, these spectral indices are designed to selected T-dwarfs with high accuracy (completeness  $>90\%$ , contamination  $<1\%$ ). The overall contamination/false positive rate for this method for spectral types of L0–L5 is  $\sim 87\%$ . A second method uses a random forest classifier to distinguish UCDs from other extragalactic contaminants or artifacts with an accuracy

score of 99.5% in cross-validation. The false positive rate of this method for spectral types of L0–L5 is  $\sim 62\%$ . Both methods rely on a training set of known UCD samples and can be combined. With these two methods, we have used these data to obtain 166 spectra of M7-T9 UCDs up to distances  $\sim 4$  kpc.

We estimated the expected number of UCDs given a galactic structure model with scale height ( $h$ ) as a free-parameter. Using a point-source limiting magnitude, we measured the effective volumes of the survey for various values of the scale height. To address intrinsic biases in our selection method, we use a Monte-Carlo simulation to reproduce a distribution of spectral type based on a set of fundamental distribution: mass function, age distribution and conversion/polynomial relation from UCD evolutionary models and our sample. We use the galactic structure model to draw a distribution of distances. With these distributions, we create a selection probability function based on sample of "degraded" templates. The final steps involve summing over selection probabilities. The predicted number of UCDs is consistent with a scale height of  $325 \text{ pc} \leq h \leq 350 \text{ pc}$ .

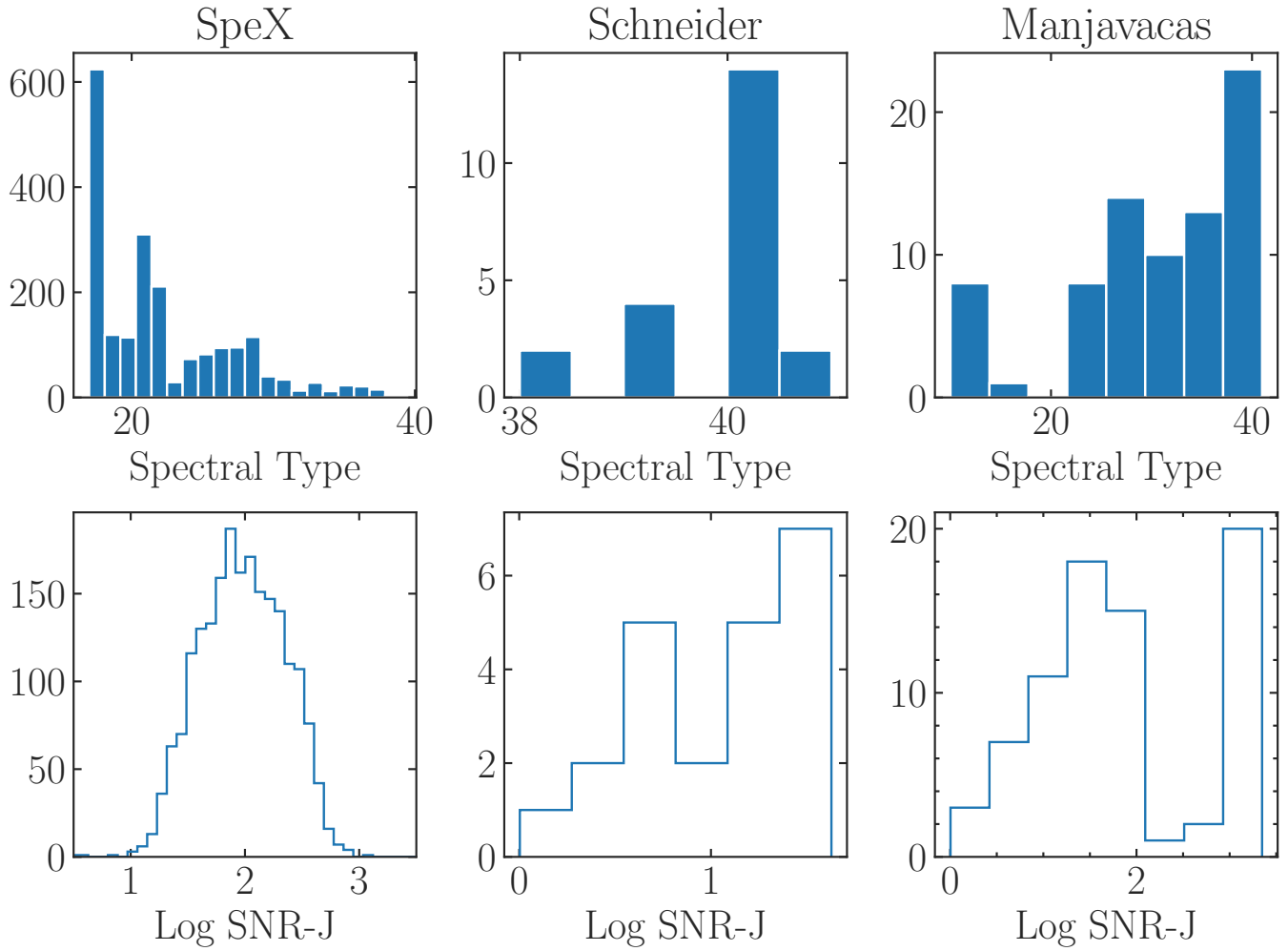
Future space missions such as JSWT, Euclid will be contaminated by UCDs. [Ryan Jr. & Reid \(2016\)](#) predicted that the number density of UCDs (M8–T8) in JSWT fields peaks around  $J \sim 24$  mag with a total surface density of  $\Sigma \sim 0.3 \text{ arcmin}^{-2}$ . With the *Large-Scale Synoptic Telescope* (LSST), and the *Wide-Field Infrared Survey Telescope* (WFIRST), we expect an increase in both sample size and spectral type accuracy, expanding the parameter space necessary to put significant constraint on the star formation history of the Milky Way in general and the mass function of UCDs in particular ([LSST Science Collaboration et al. 2009](#), [Spergel et al. 2015](#)).

## ACKNOWLEDGMENTS

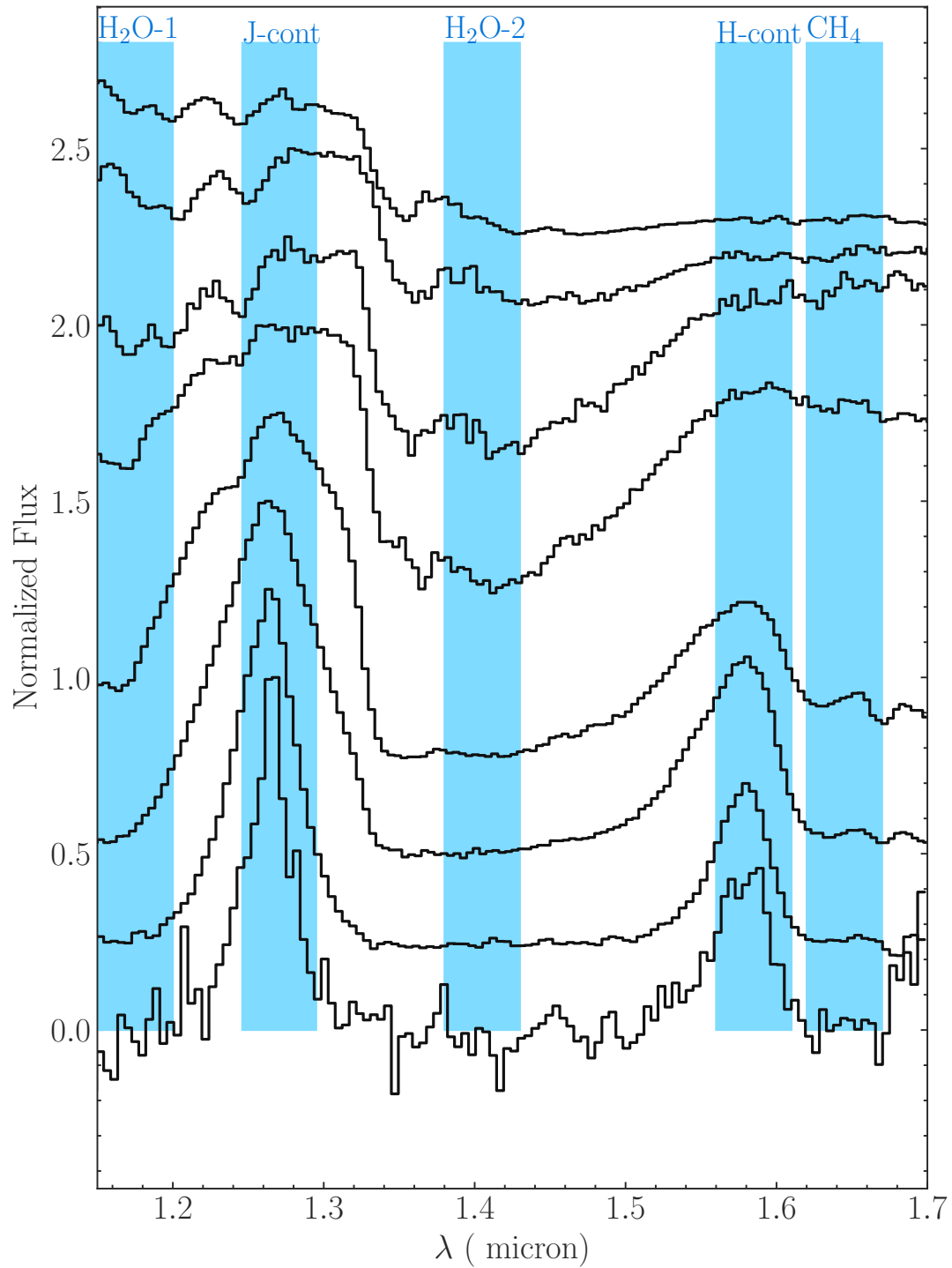
This work is based on observations taken by the 3D-HST treasury program (GO 12177 and 12328) with the NASA/ESA HST, which is operated by the Association of universities for Research in Astronomy, Inc. under NASA contract NAS5-26555.

CA thanks the LSSTC Data Science Fellowship Program, which is funded by LSSTC, NSF Cyber-training Grant #1829740, the Brinson Foundation, and the Moore Foundation; his participation in the program has benefited this work.

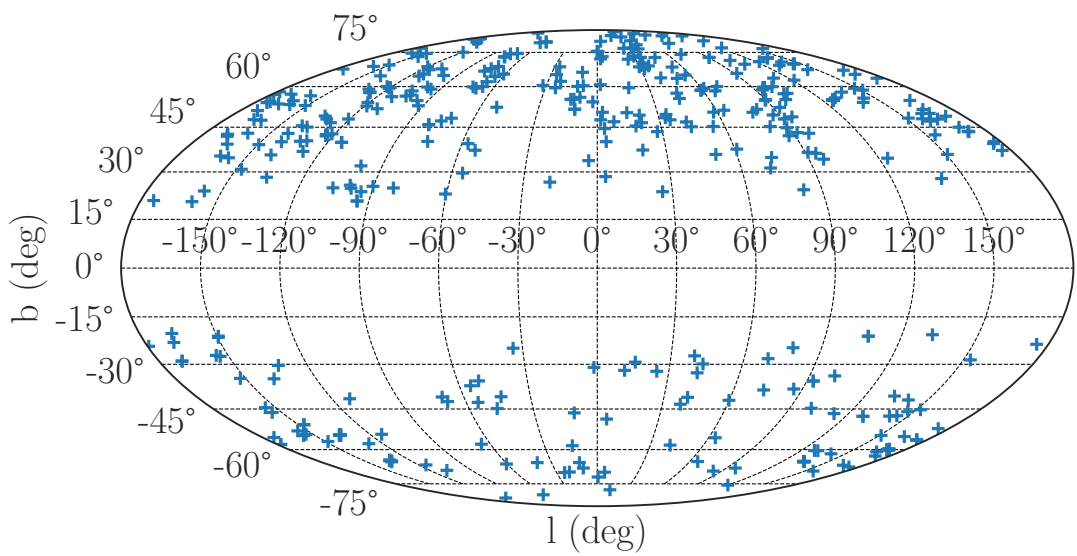
*Software:* Astropy([Collaboration et al. 2013](#)), Matplotlib ([Hunter 2007](#)), SPLAT([Burgasser 2014b](#)), Scipy([Virtanen et al. 2019](#)), Pandas, Seaborn ([Waskom et al. 2014](#)), Daft, Pymc3([Salvatier et al. 2016](#))



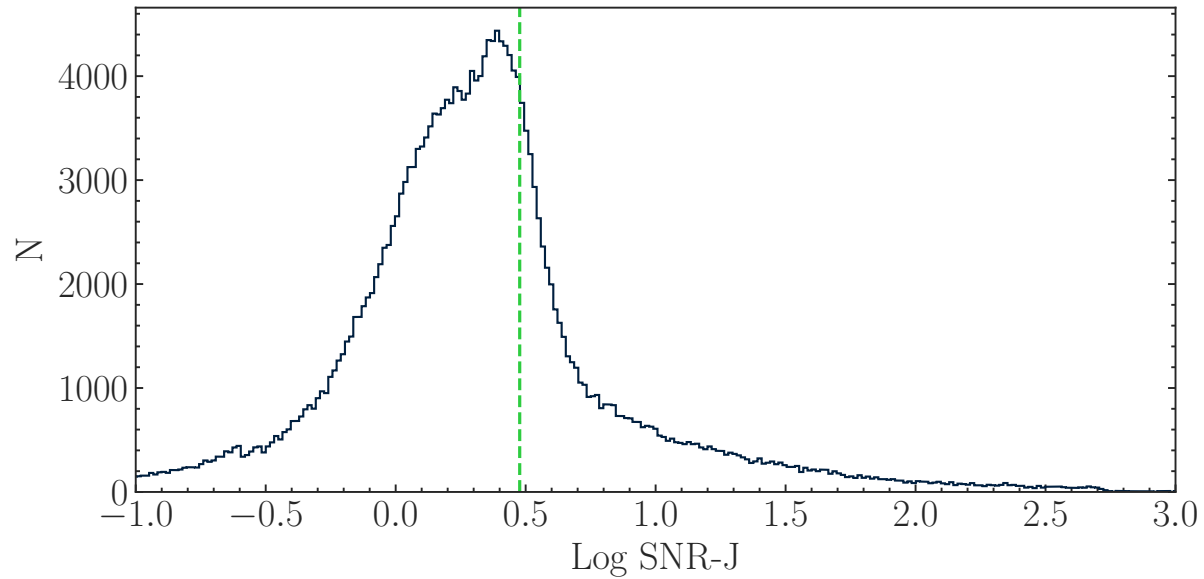
**Figure 1.** Distribution in spectral type and signal to noise of three calibration samples of UCDs used in this study



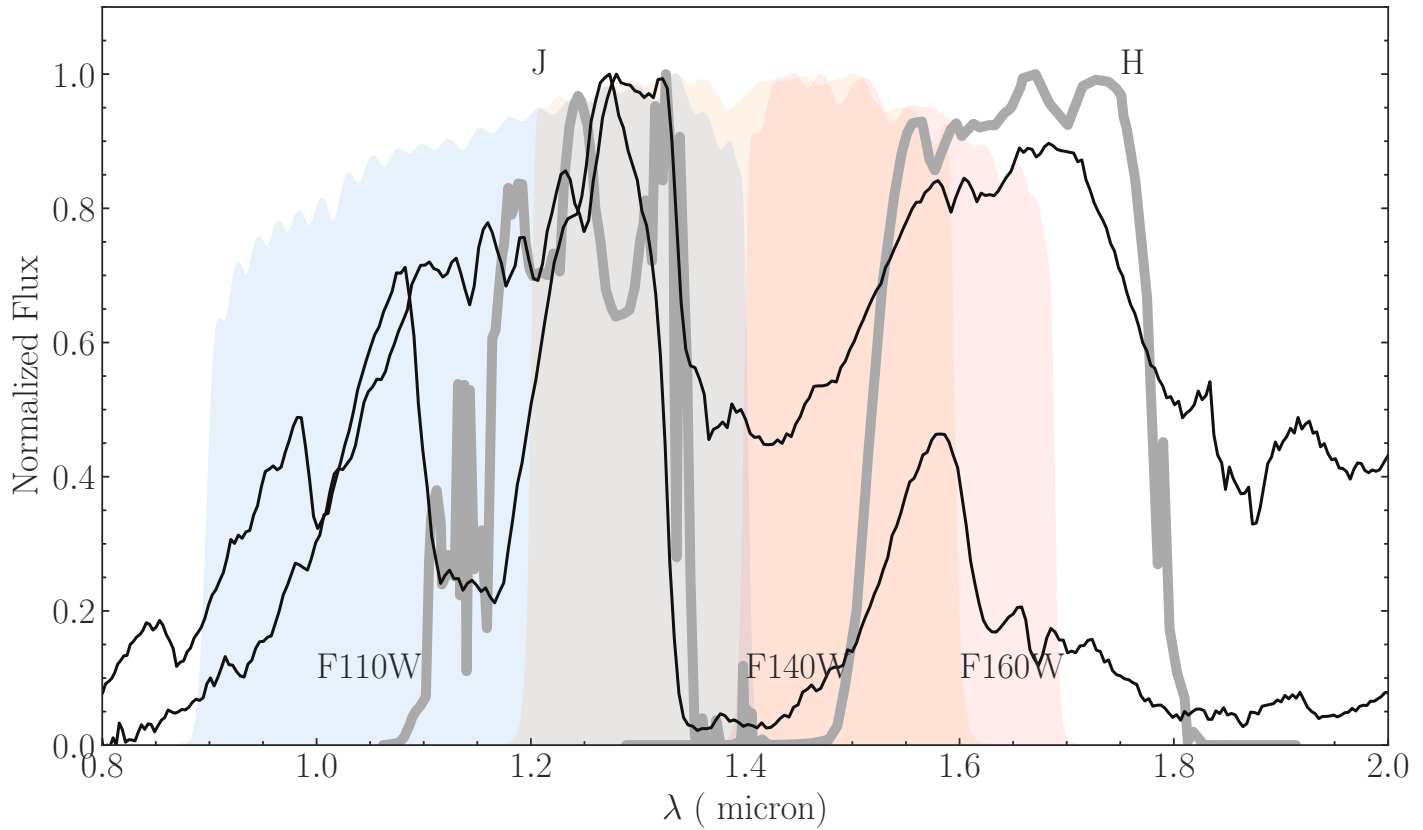
**Figure 2.** M5-T9 low resolution SpeX spectral standards (Kirkpatrick et al. 2010) with highlighted bands showing the definition of spectral indices used in this study



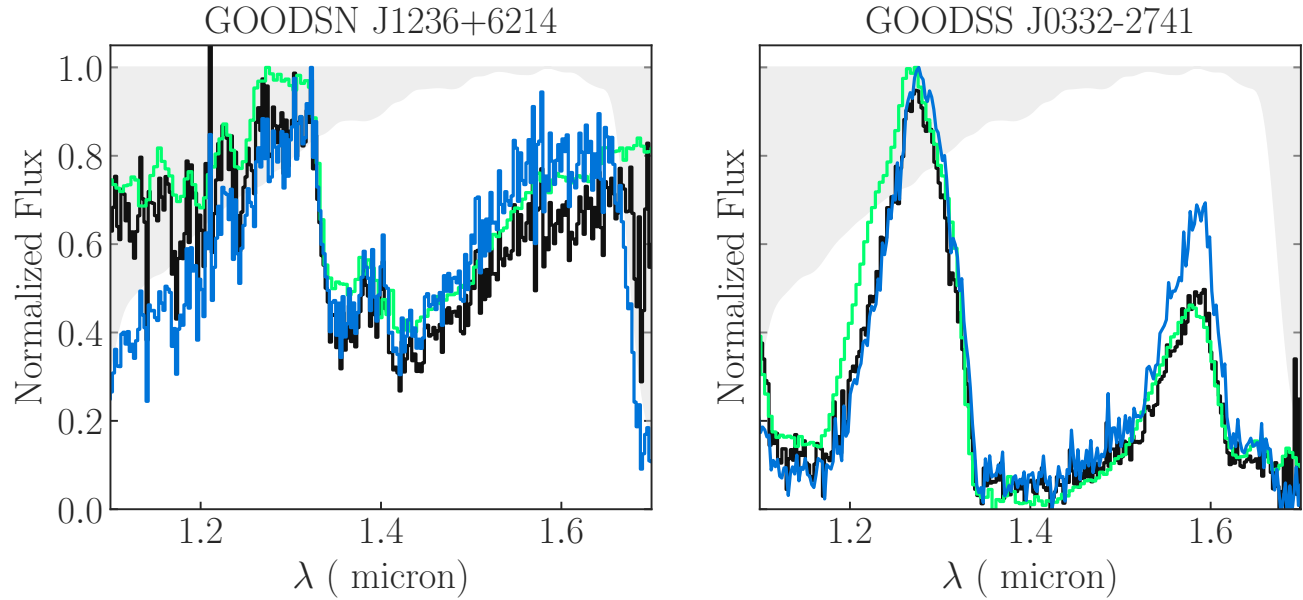
**Figure 3.** Sky distribution all the pointings in WISPS and 3D-HST used in this study



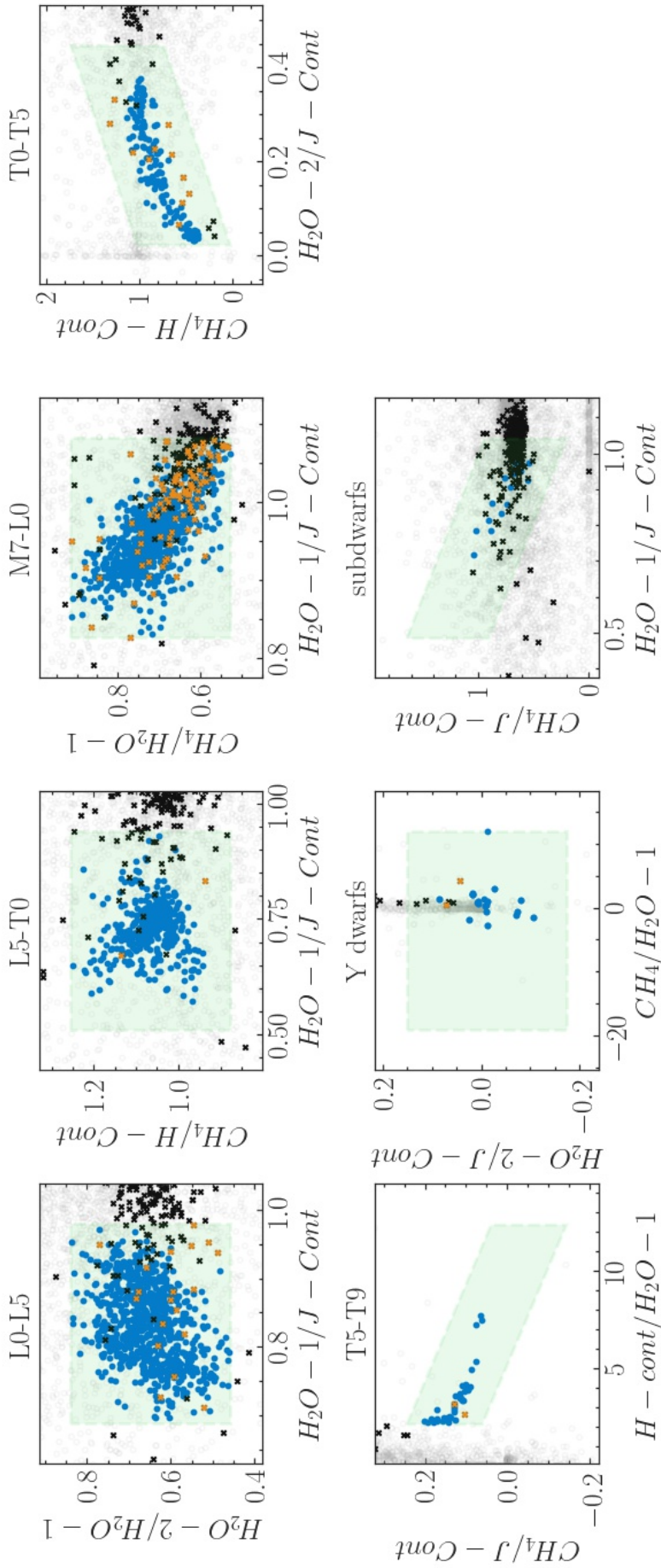
**Figure 4.** F-test and SNR-J distributions of all Spectra in both surveys showing the cuts at 0.4 and 3 respectively



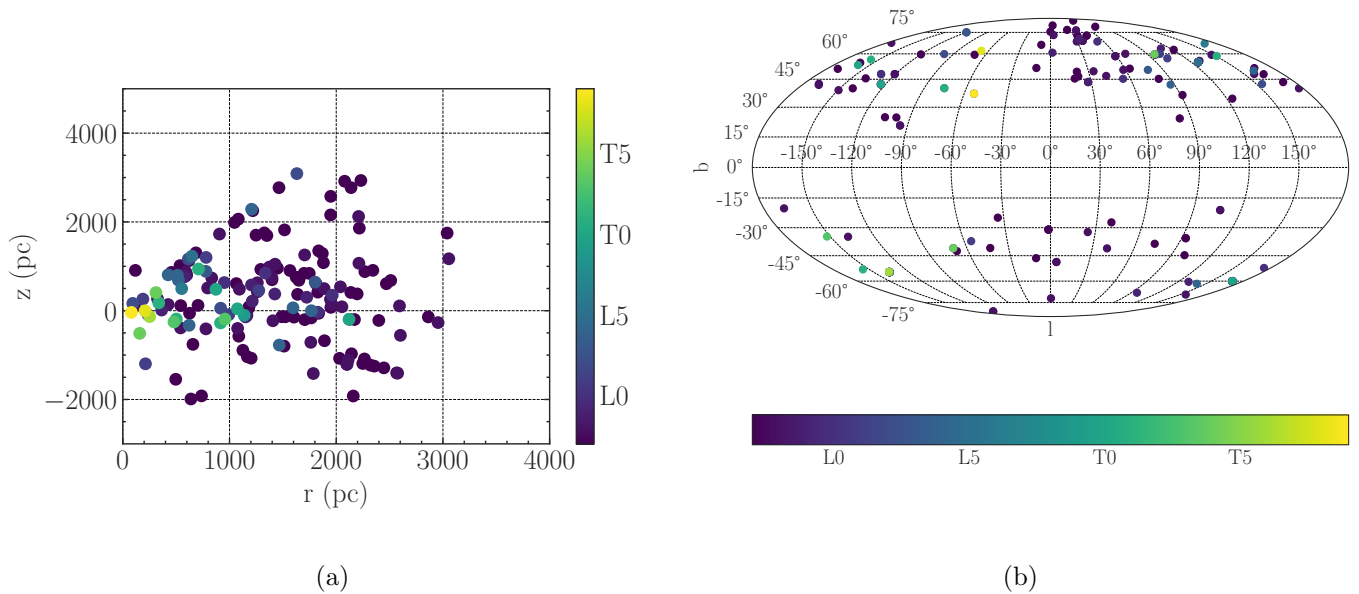
**Figure 5.** Comparison between spectral coverage of different WFC3 and 2MASS filters used in this study. We used these filters to estimate absolute magnitudes of our UCD sample



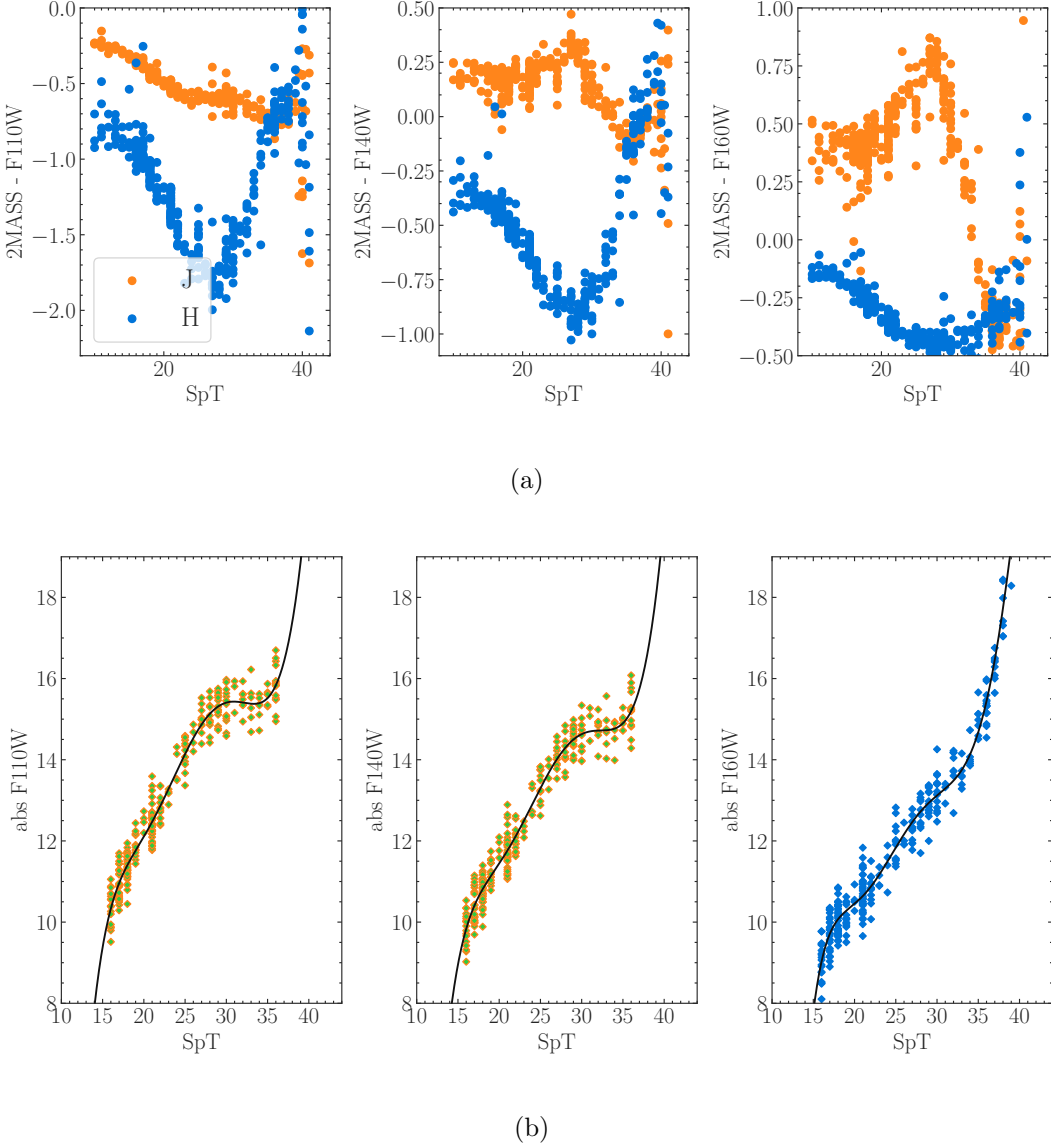
**Figure 6.** Example of 2 HST-3D spectra before and after continuum correction to obtain the correct slope. The sensitivity curve is plotted in grey.



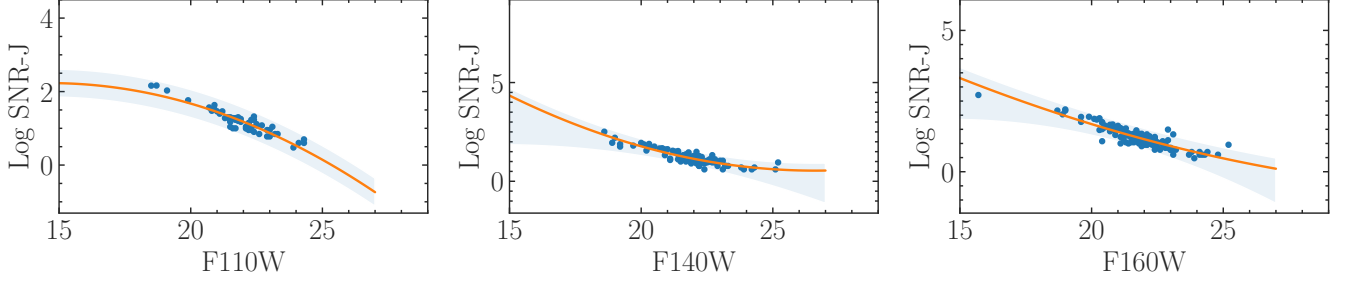
**Figure 7.** Best selection criteria for different subtype ranges. The grey points are the contaminants after we applied both a J-SNR cut and and F-test cut, the blue points are the set of templates (from the calibration samples) used to define these boxes. The crossed black points are the real UCDs confirmed after visual inspection and the orange crosses are the UCDs that have spectral types for each particular box (e.g a L2 UCD would be colored orange in the L0-L5 while an L7 would be colored black the L0-L5 box )



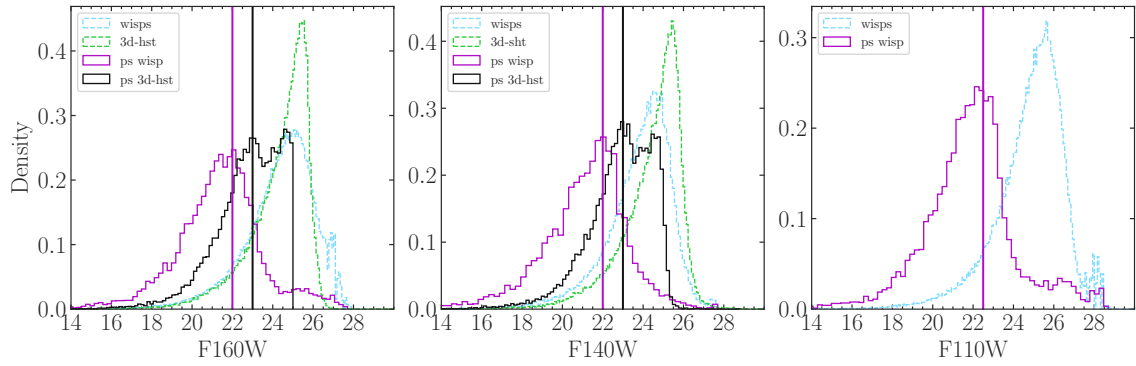
**Figure 8.** (a) Distance distribution of the UCD sample (b) Galactic distribution of the UCD sample



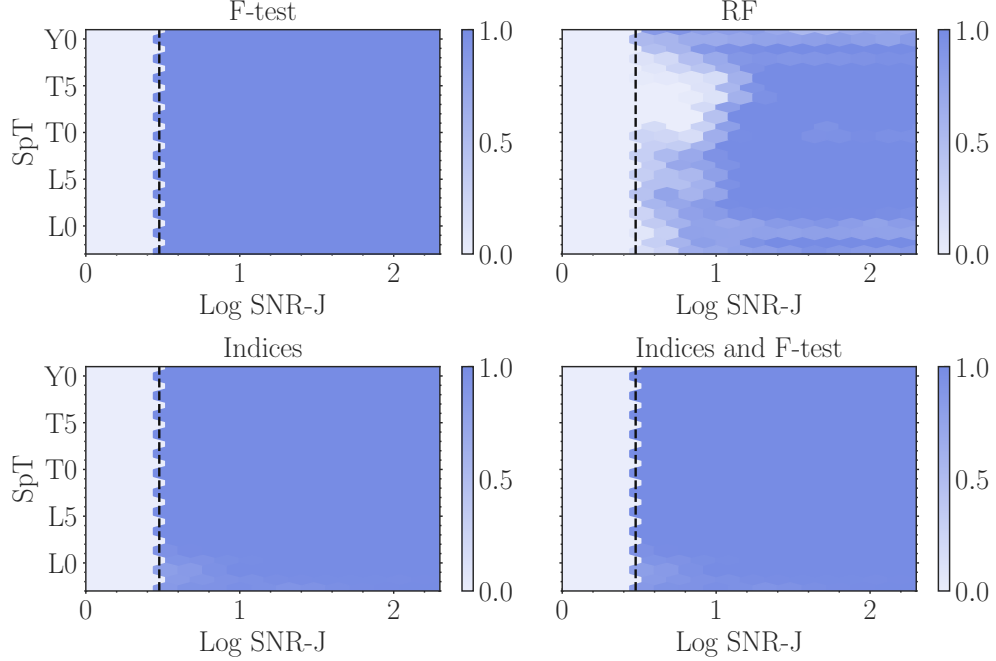
**Figure 9.** (a) Offsets between 2MASS J, H magnitudes and HST F110W, F140W, F160W magnitudes as a function of spectral type (b) Absolute magnitude-spectral type relations for HST and 2 MASS filters. For HST filters, the dotted green curve shows the derived relation using only the offset between the respective HST filter and 2MASS J filter while the blue curve shows the derived relation using the offset with the 2MASS H filter. The solid line shows a best-fit 6th-order polynomial used, considering the wavelength coverage of the respective filters (figure 5). We report the coefficients of these polynomials in table 3



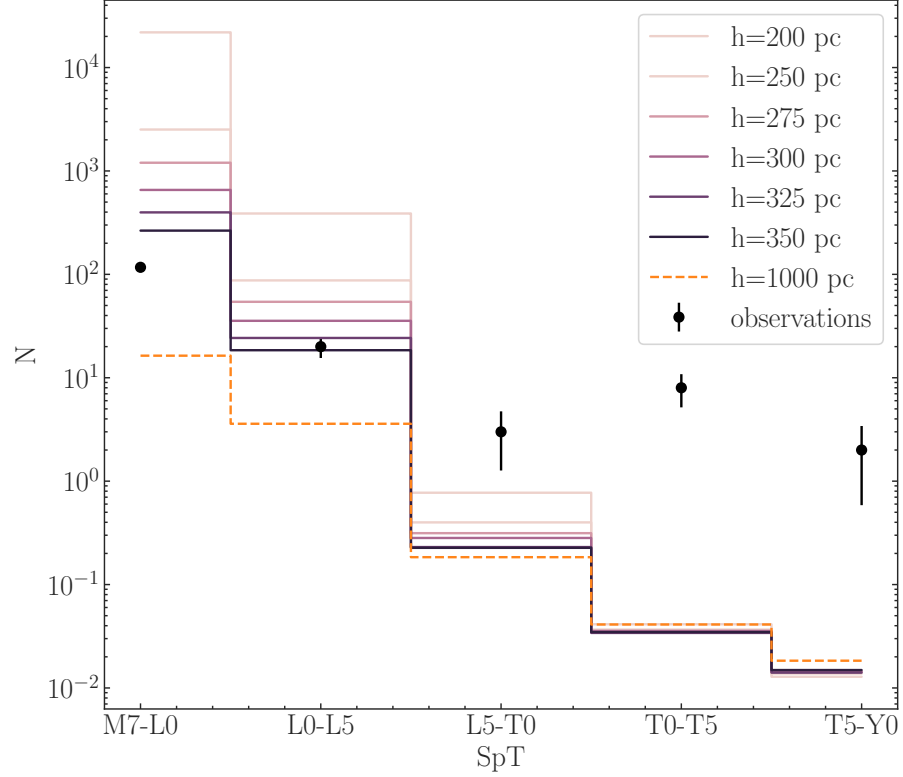
**Figure 10.** Linear fits between SNR-J and apparent F110W, F140W, F160W magnitudes using the sample of UCDs. These relations are reported in table 3 and used to estimate SNR-J for different apparent magnitudes



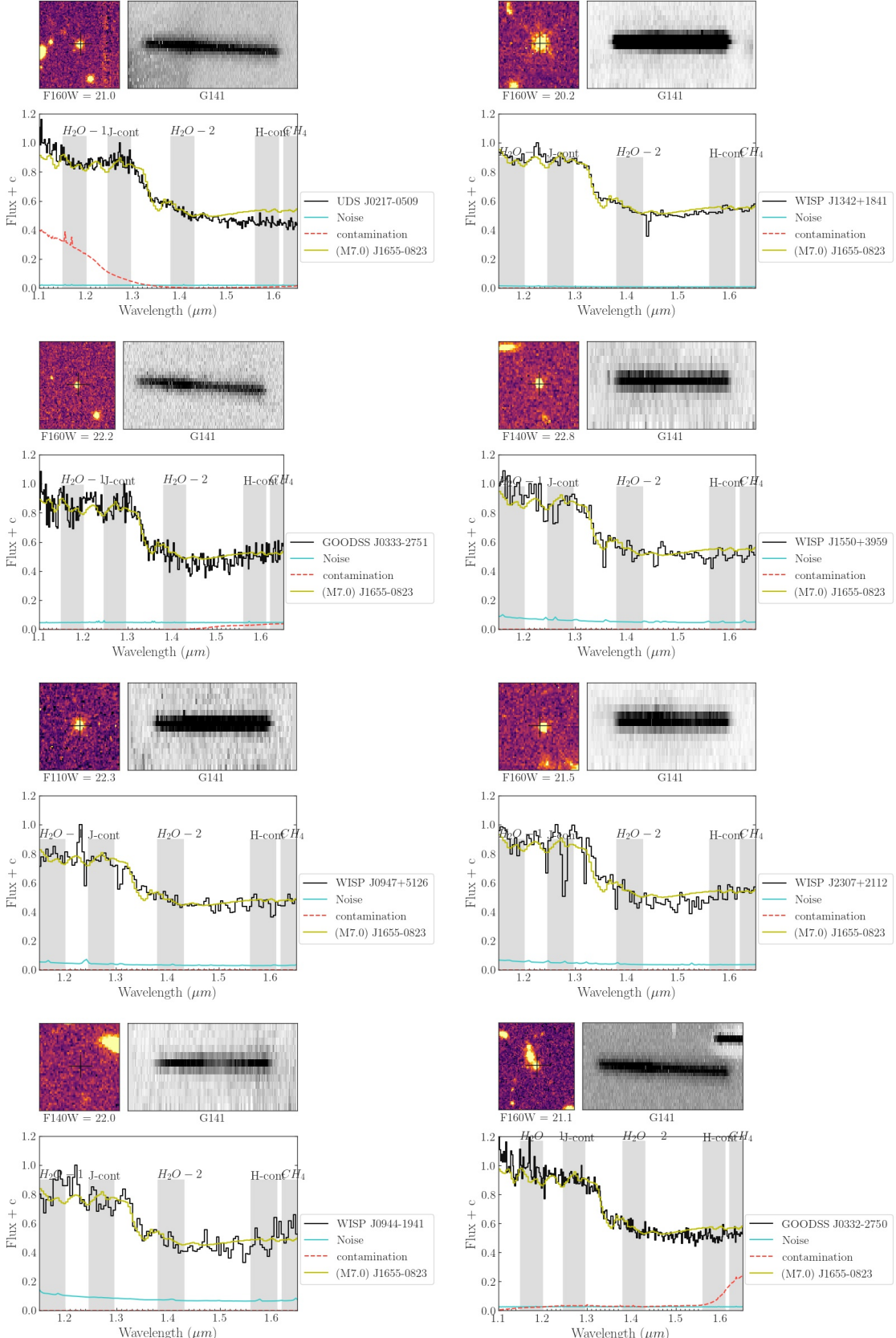
**Figure 11.** Magnitude distribution of point sources (solid lines) and all the sources (dotted lines) in both WISP & 3D-HST. We estimate the limiting magnitudes based on the distribution of point sources. For wisps the limiting magnitudes are F110W=22.0, F140W= 21.5, and F160W= 21.5. For 3D-HST the limiting magnitudes are F140W=22.5 and F160W. These magnitudes are used to compute the effective volumes for each spectral type



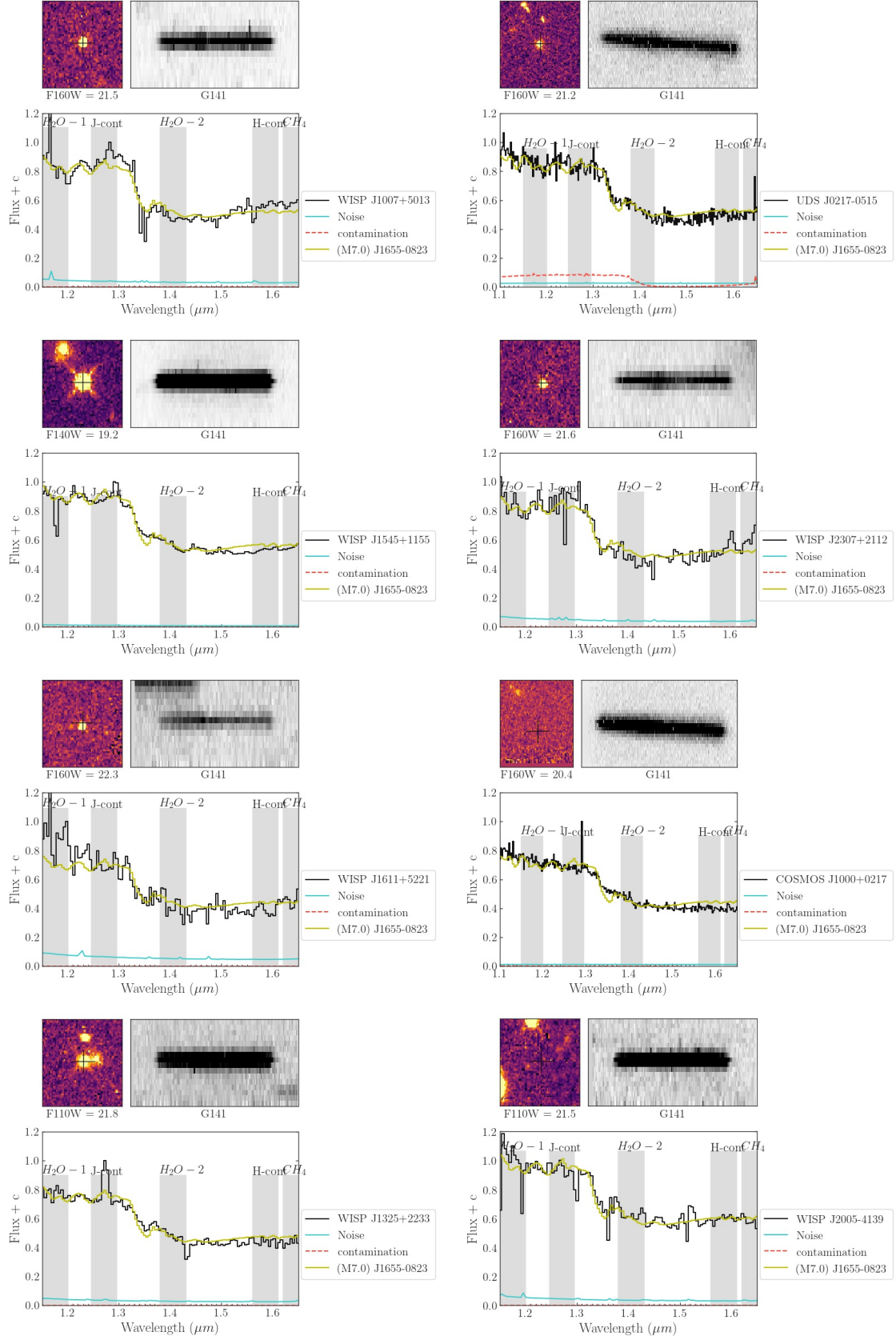
**Figure 12.** Visualization of our selection function as a function accross spectral type and SNR-J. The label "F-test" indicates spectra with  $F\text{-test} < 0.4$ , the label "RF" indicates the spectra labelled as UCDs by the random forest classifier, and the label "Indices" indicates the spectra selected by our best selection criteria. The bar indicates the selection probability defined as the number of spectra selected over the total number of spectra in each SNR-J, spectral type bin. In the Monte-Carlo simulation, we use the most-selective selection function.

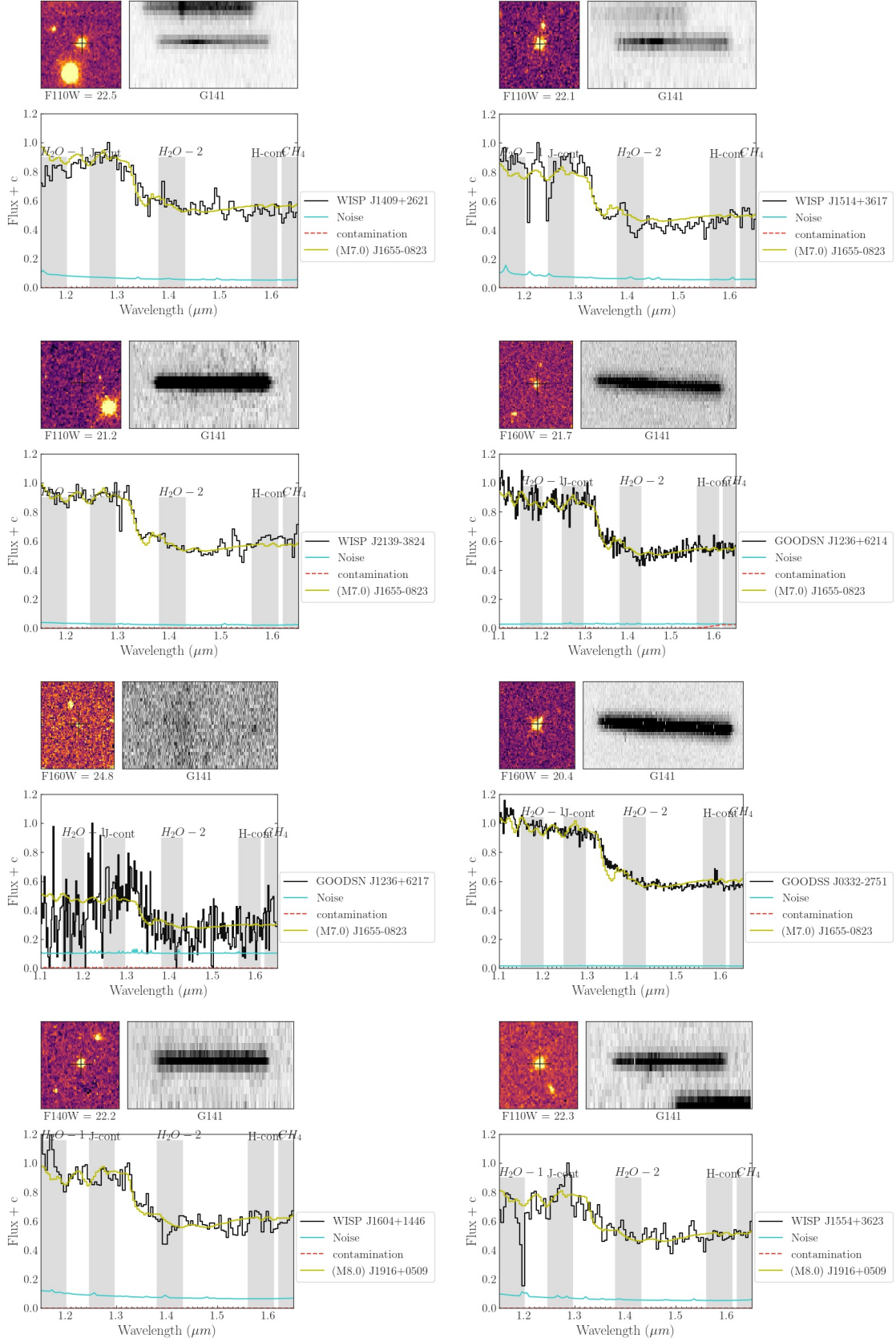


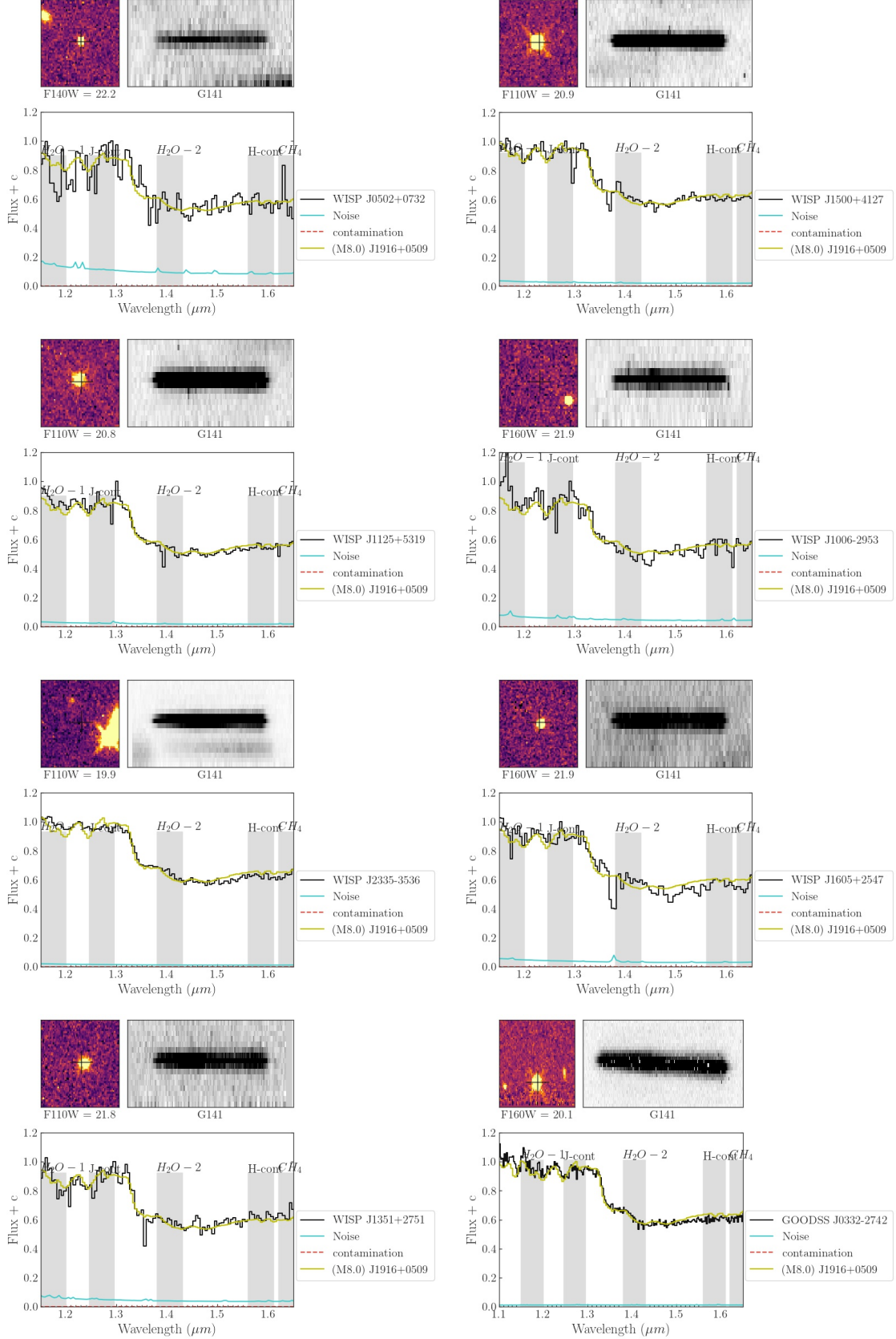
**Figure 13.** Comparison between the measured number densities and the expected number densities based on the Monte-Carlo simulation based on different age distributions. These estimates are based on limiting magnitude F140W <21.5 and SNR-J>10 which eliminates most of our T dwarf sample

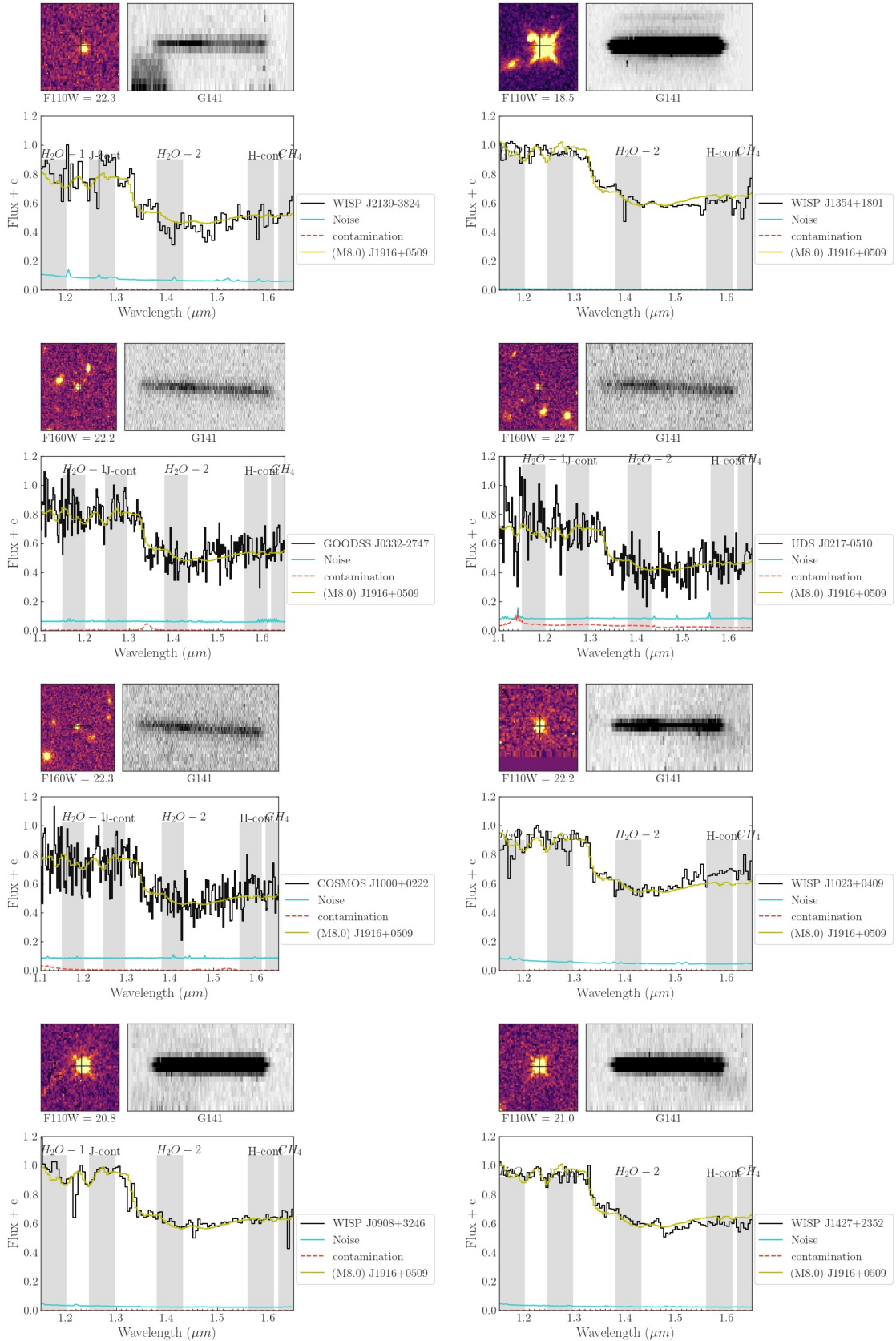


**Figure 14.** Spectra of UCDs in both surveys. The bottom plot shows the 1D spectrum fit to a spectral standard, The noise and the contamination are also shown, the top left plot shows the WFC3 image acquired in either F140W, F160W or F110W filter and the top-right plot shows the cutoff of the G141 spectrum for that extracted object.

**Figure 15.** cont.

**Figure 16.** cont.

**Figure 17. cont.**

**Figure 18.** cont.

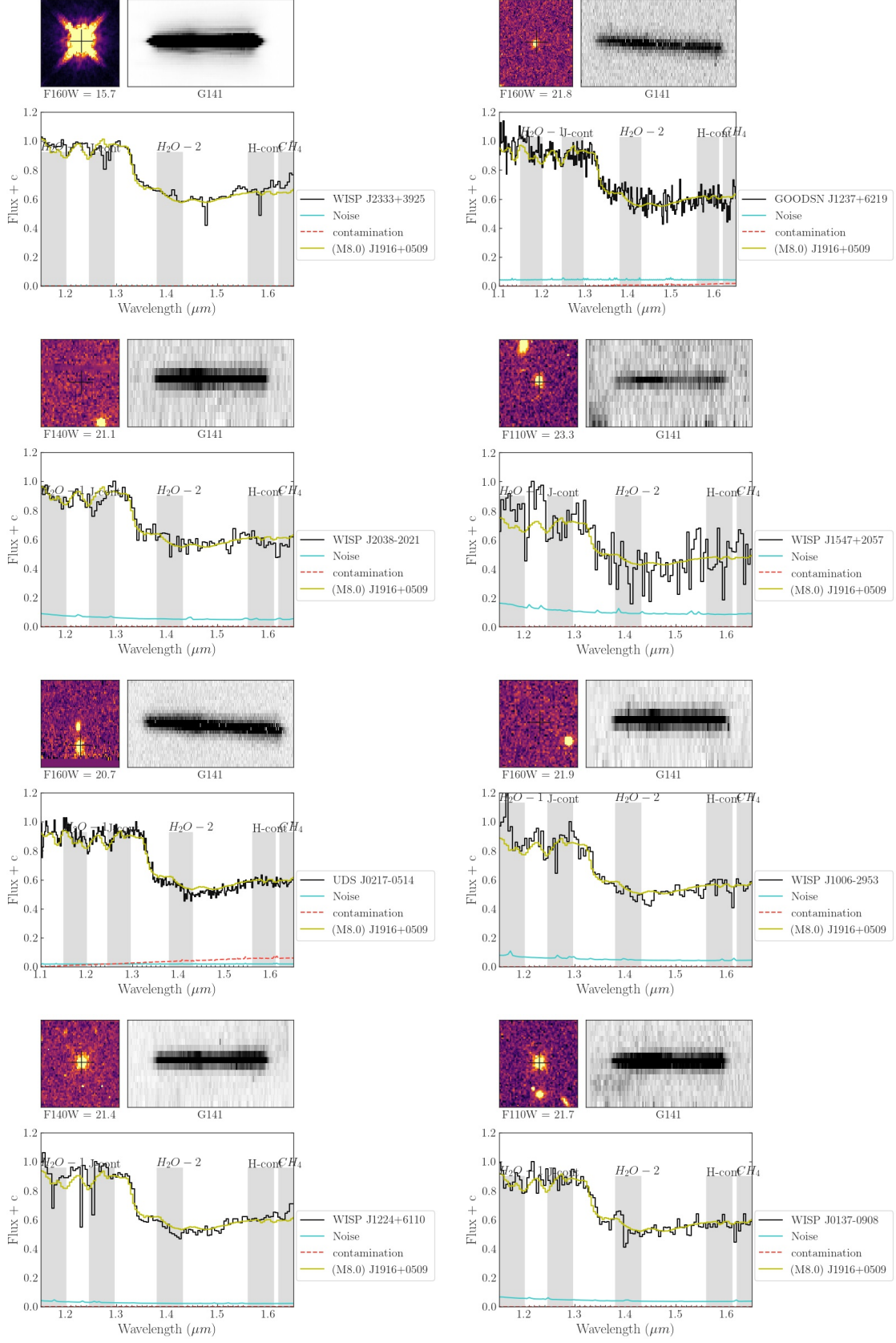
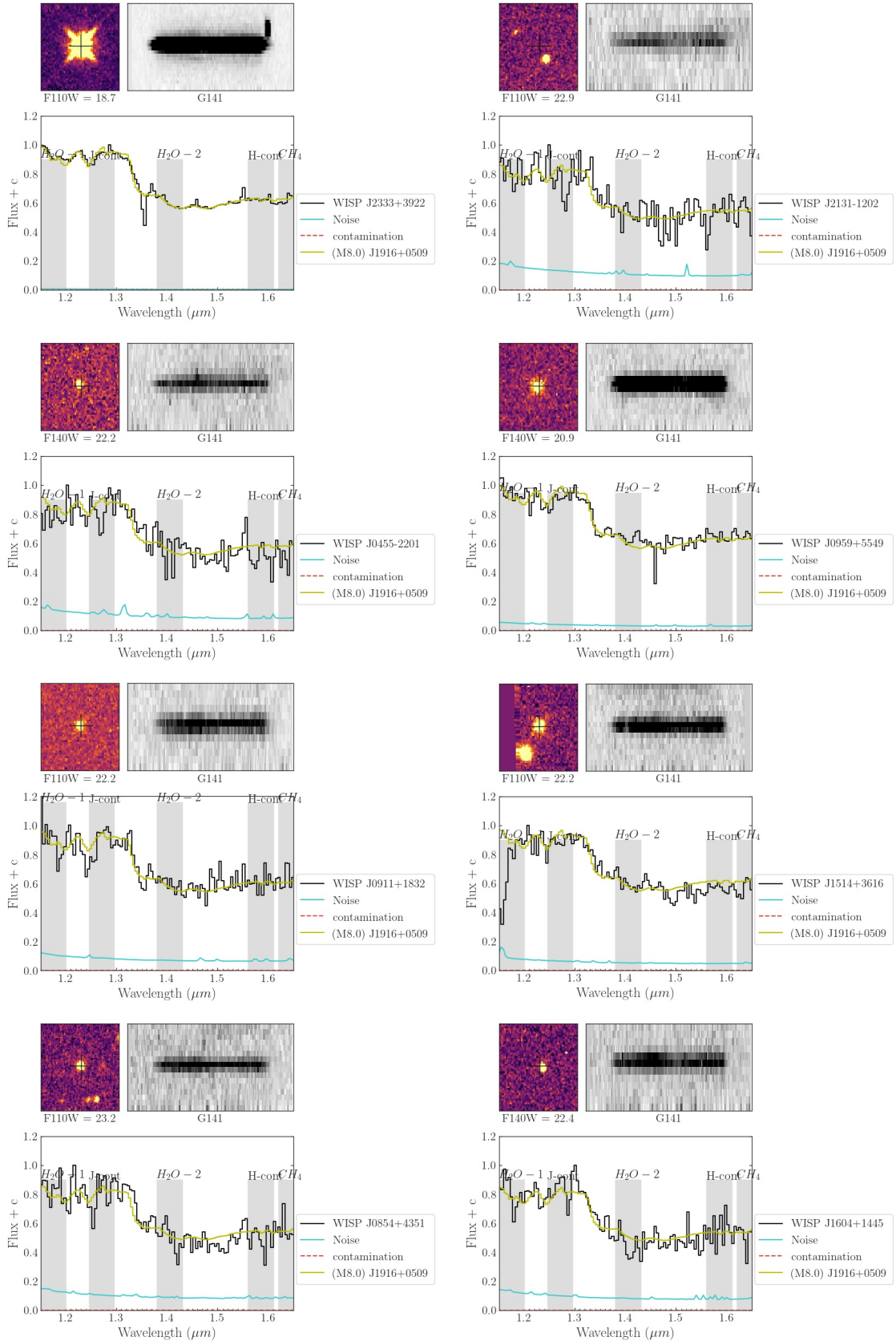
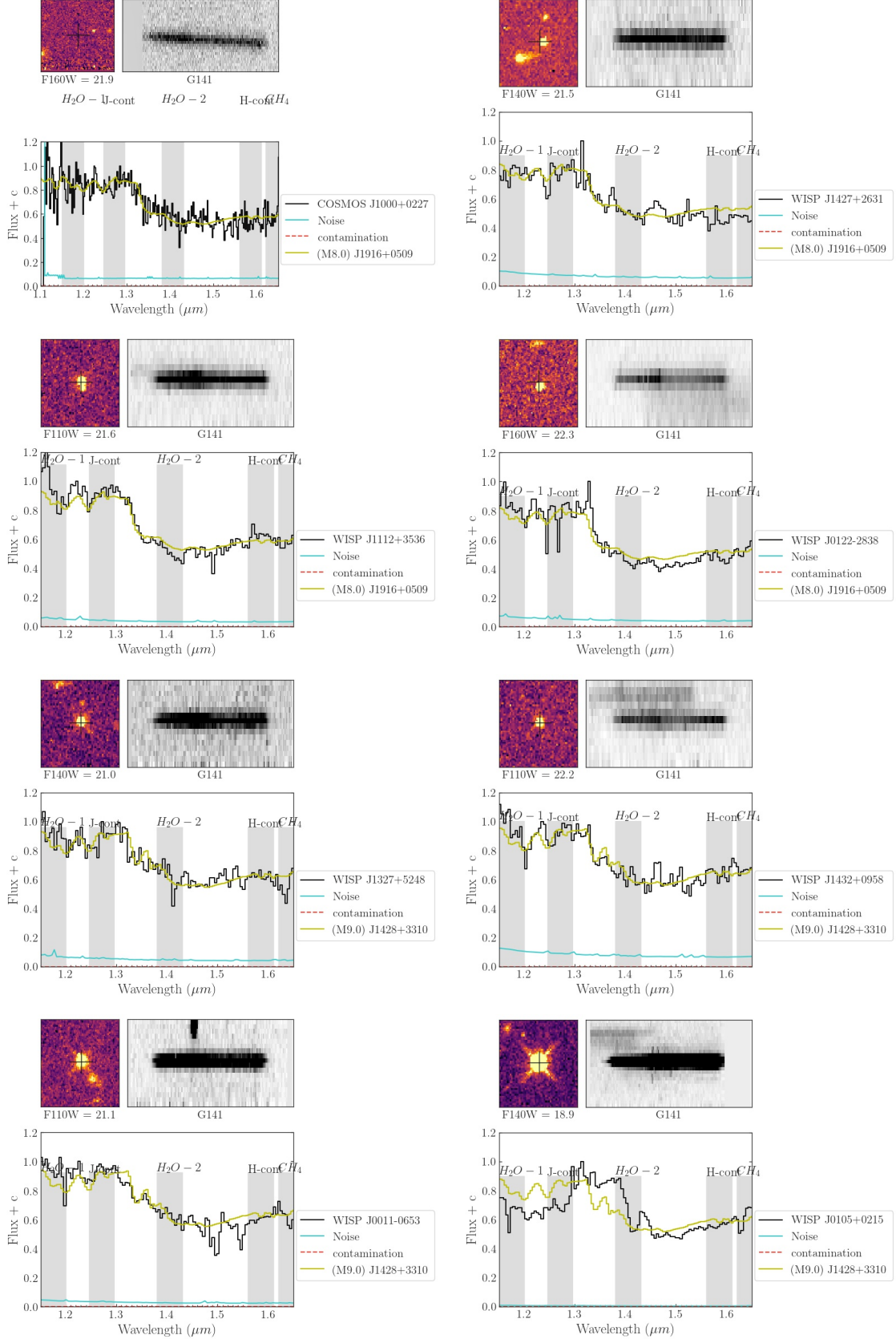
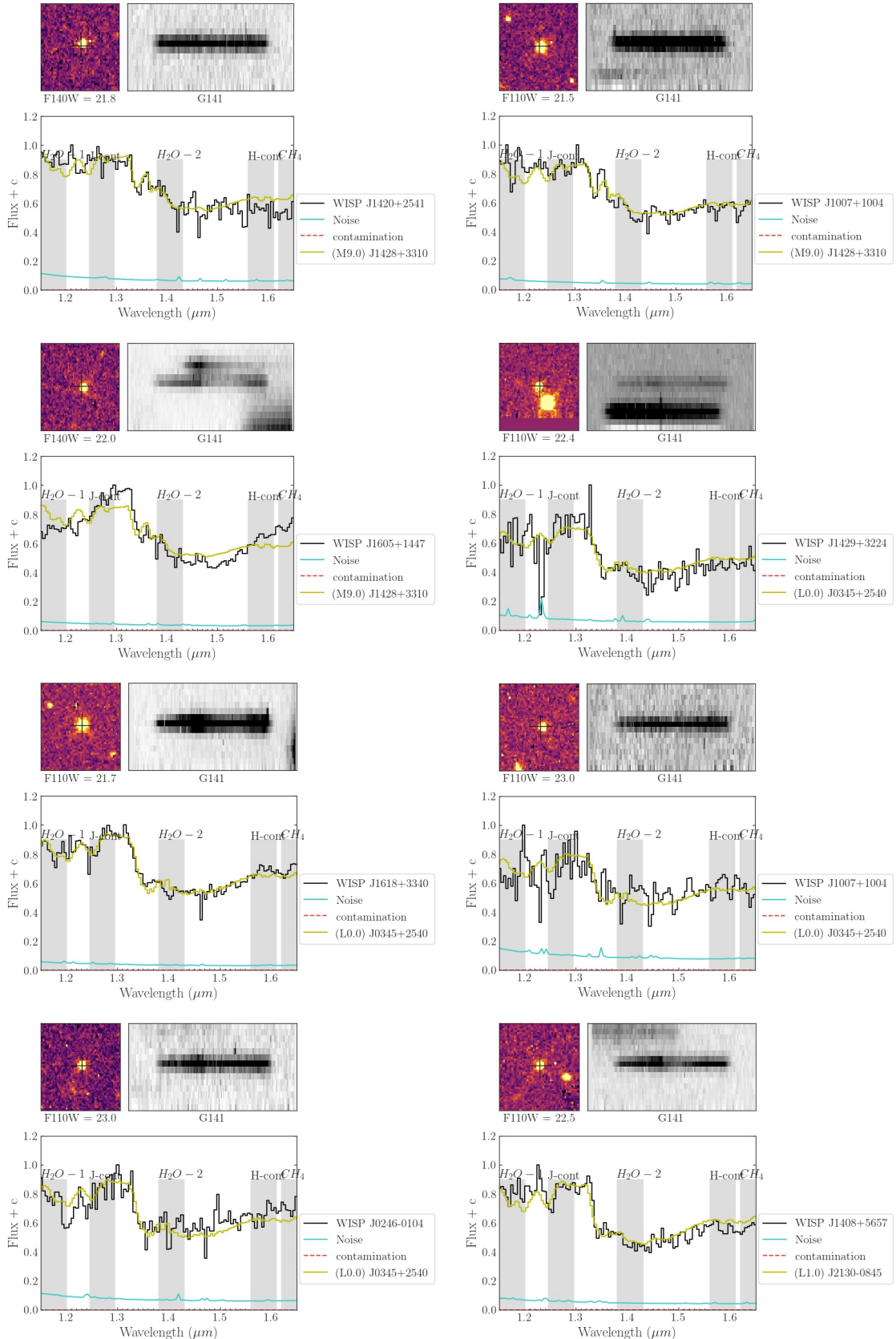
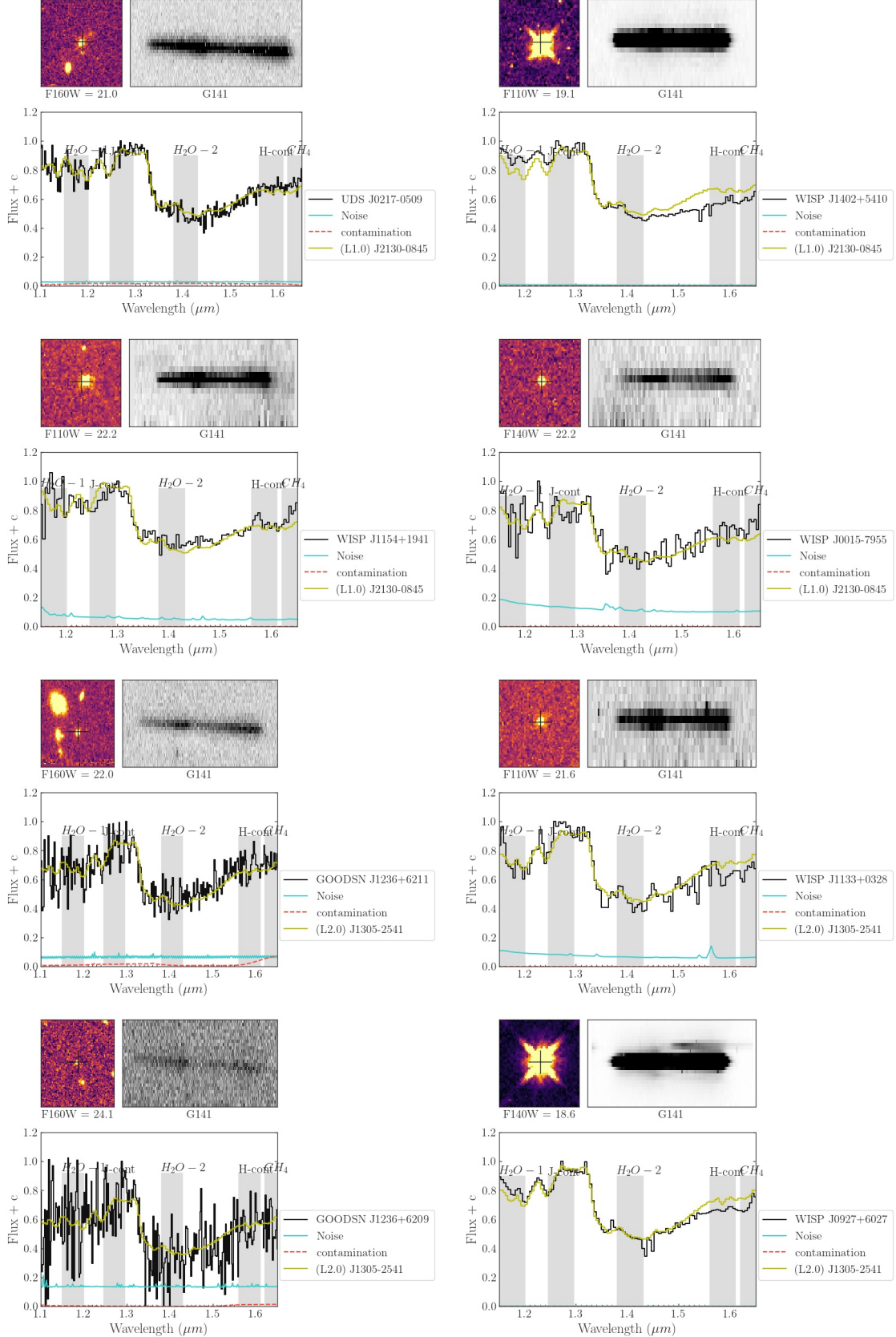


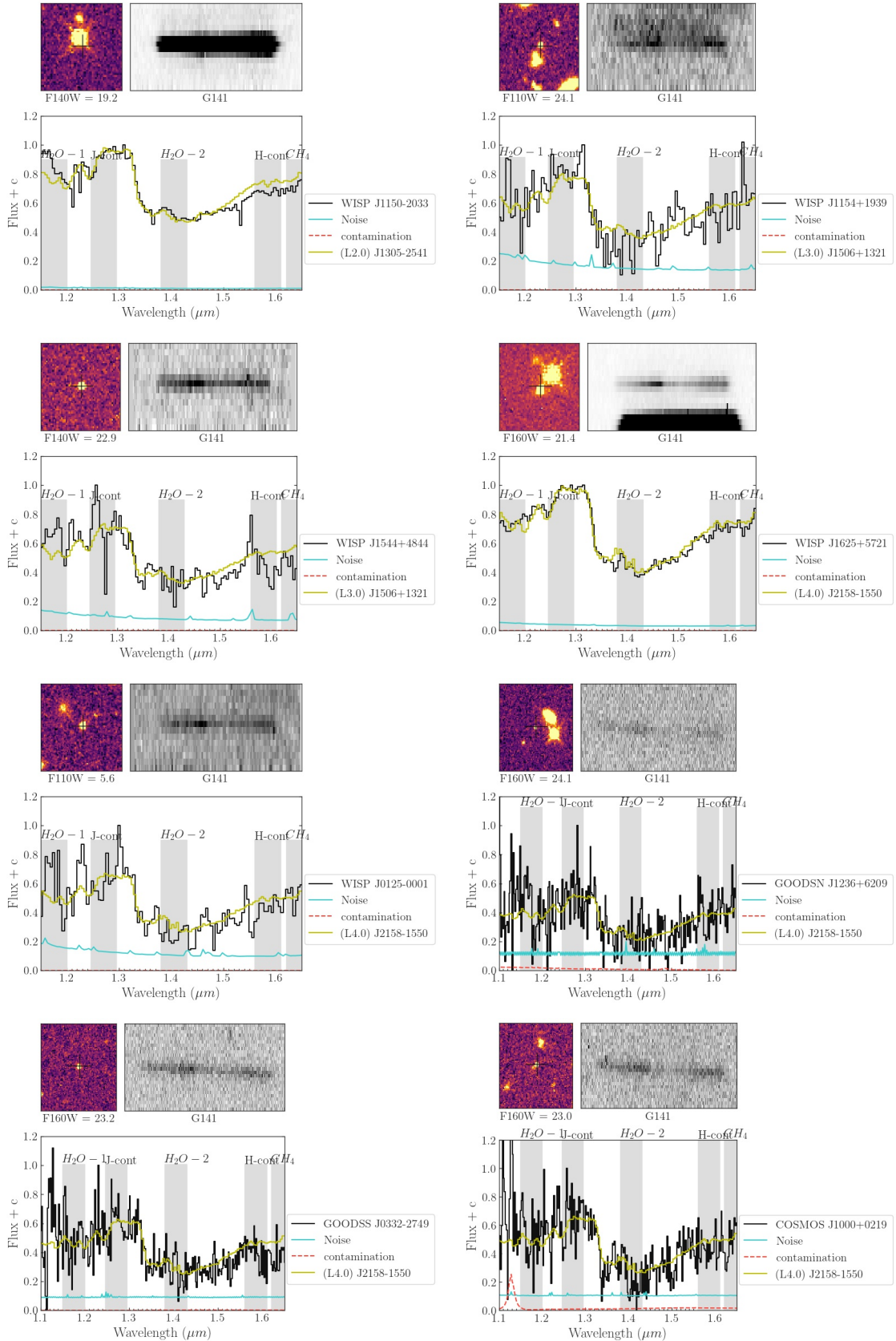
Figure 19. cont.

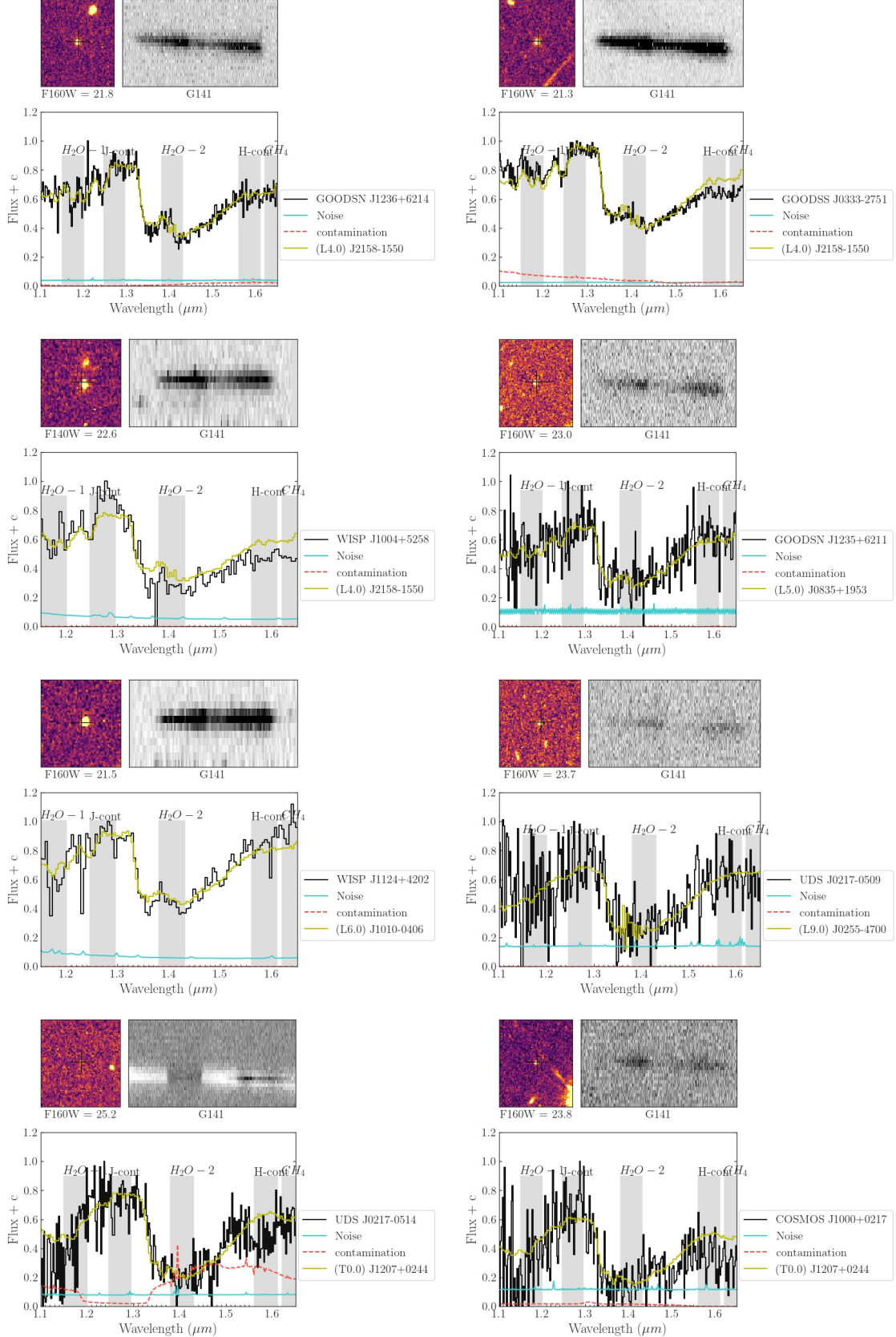
**Figure 20.** cont.

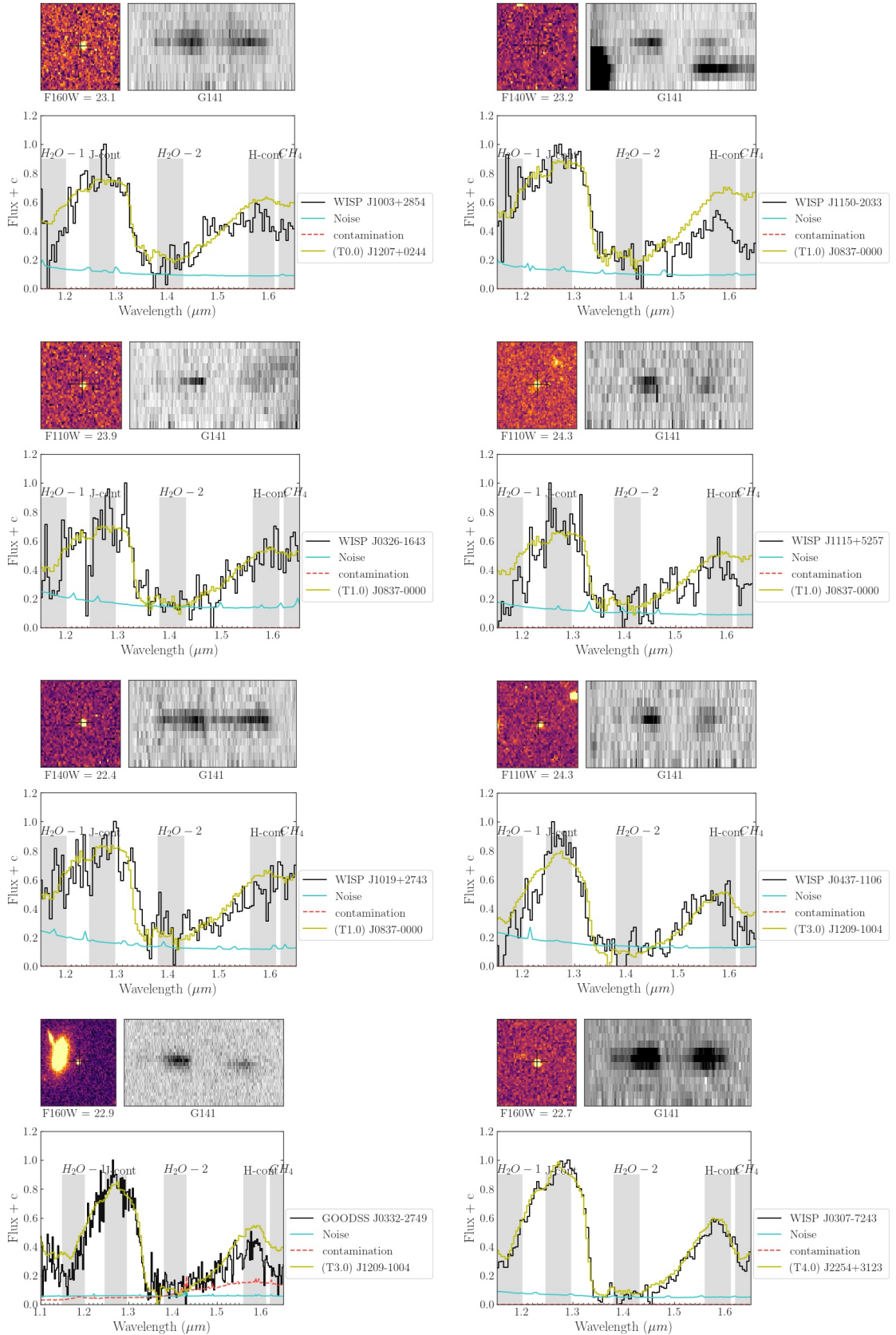
**Figure 21.** cont.

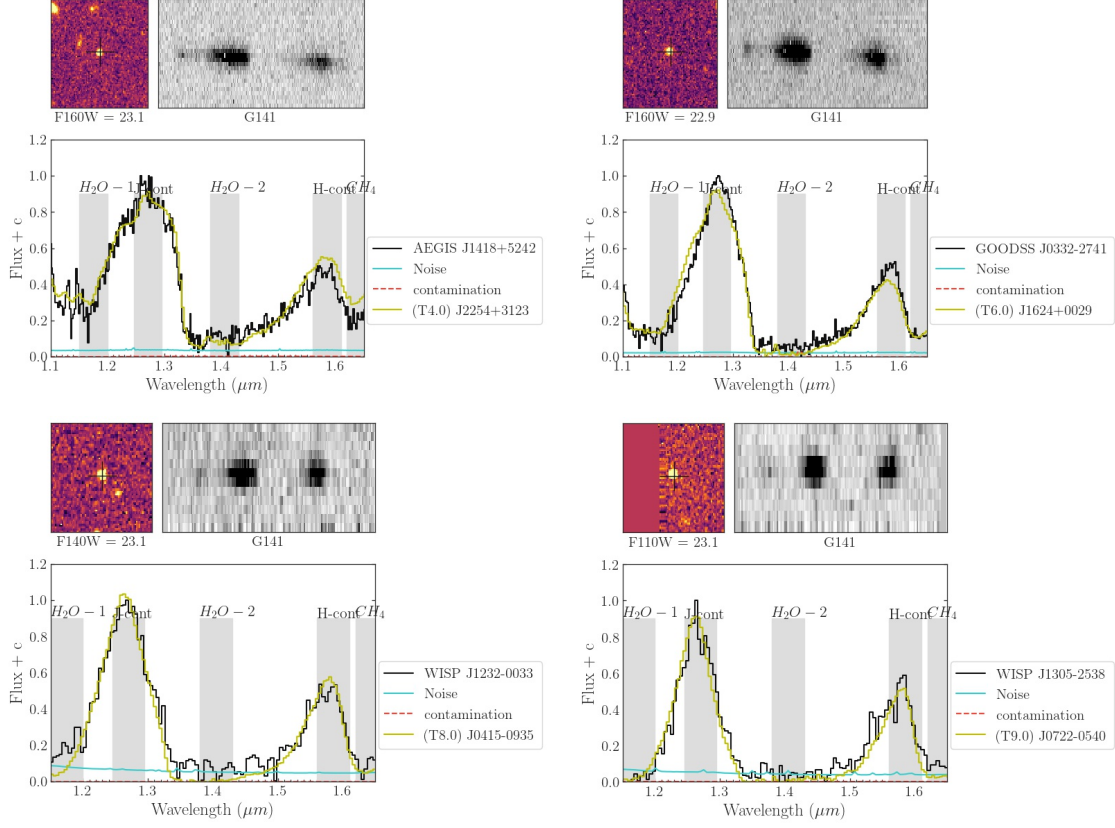
**Figure 22.** cont.

**Figure 23.** cont.

**Figure 24.** cont.

**Figure 25. cont.**

**Figure 26.** cont.

**Figure 27.** cont.**Table 1.** Selection Criteria

SpT Range	X-axis	Y-axis	v1	v2	v3	v4	CP	CT	FP
L0-L5	H <sub>2</sub> O-1/J-Cont	H <sub>2</sub> O-2/H <sub>2</sub> O-1	(0.69, 0.84)	(0.98, 0.84)	(0.98, 0.46)	(0.69, 0.46)	0.97	0.075	0.93
L5-T0	H <sub>2</sub> O-1/J-Cont	CH <sub>4</sub> /H <sub>2</sub> O-1	(0.51, 7.21)	(0.94, 7.21)	(0.94, -4.5)	(0.51, -4.5)	0.98	0.209	0.95
M7-L0	H <sub>2</sub> O-1/J-Cont	CH <sub>4</sub> /J-Cont	(0.83, 0.83)	(1.08, 0.83)	(1.08, 0.54)	(0.83, 0.54)	0.97	0.135	0.86
T0-T5	H <sub>2</sub> O-1/J-Cont	CH <sub>4</sub> /H-Cont	(0.23, 0.96)	(0.93, 1.74)	(0.93, 0.75)	(0.23, -0.04)	0.97	0.165	0.95
T5-T9	H-cont/H <sub>2</sub> O-1	CH <sub>4</sub> /J-Cont	(2.16, 0.24)	(12.39, 0.04)	(12.39, -0.14)	(2.16, 0.06)	0.95	0.001	0.71
Y dwarfs	CH <sub>4</sub> /H <sub>2</sub> O-1	H <sub>2</sub> O-2/J-Cont	(-18.94, 0.15)	(12.03, 0.15)	(12.03, -0.17)	(-18.94, -0.17)	0.88	0.061	0.99
subdwarfs	H <sub>2</sub> O-2/J-Cont	CH <sub>4</sub> /H-Cont	(0.18, 1.17)	(0.75, 1.17)	(0.75, 0.86)	(0.18, 0.85)	0.89	0.163	0.91

**Table 2.** List of L0-T9 UCDs

ShortName	GrismID	SNR-J	SpT	RA	DEC	F110W	F140W	F160W	Distance(pc)	Distance(kpc)
WISP1545+0933	PAR138-00108	7	M7	236.393112	9.559070	22.8			4248	106

**Table 2** continued on next page

**Table 2** (*continued*)

ShortName	GrismID	SNR_J	SPT	RA	DEC	F110W	F140W	F160W	Distance(pe)	Distance
WISP1325+2233	PAR436-00037	20	M7	201.376205	22.555500	21.8		21.2	1615	465
WISP1354+1801	PAR361-00004	145	M7	208.564117	18.033100	18.5		19.0	492	234
GOODSN1236+6214	GOODSN-13-G141_20147	29	M7	189.076431	62.240665		21.8	21.7	2385	216
WISP1420+2541	PAR301-00038	9	M7	215.205597	25.691600		21.9		2285	61
WISP2005-4139	PAR371-00045	19	M7	301.436218	-41.656000	21.3		21.2	1478	552
WISP1023+0409	PAR347-00017	37	M7	155.843842	4.156480	20.7		20.5	1076	380
WISP1703+6136	PAR155-00040	22	M7	255.800537	61.614300			21.6	2495	63
WISP0122-2837	PAR128-00034	16	M7	20.700928	-28.631500			21.9	2858	70
UDS0216-0513	UDS-21-G141_14877	41	M7	34.248672	-5.227246		20.9	20.8	1583	139
WISP2307+2112	PAR166-00044	15	M7	346.819458	21.202500			21.6	2452	62
GOODSS0333-2751	GOODSS-28-G141_12490	18	M7	53.262383	-27.853979		22.0	22.2	2785	376
WISP1305-2538	PAR32-00044	17	M7	196.330322	-25.638200	22.4	22.0	22.4	2487	815
WISP0307-7245	PAR130-00076	8	M7	46.930344	-72.760500			22.4	3595	90
COSMOS1000+0212	COSMOS-14-G141_02407	23	M7	150.114136	2.203750		21.4	21.4	2052	212
WISP1303+2952	PAR35-00023	43	M7	195.952576	29.867760	20.9	20.8	20.5	1224	317
AEGIS1419+5253	AEGIS-11-G141_37605	23	M7	214.830063	52.883358		21.7	21.7	2339	190
WISP2307+2112	PAR166-00041	17	M7	346.821686	21.208400			21.5	2373	58
UDS0217-0508	UDS-05-G141_41125	36	M7	34.384212	-5.136668		20.9	20.9	1635	170
WISP1102+1053	PAR11-00046	11	M7	165.566360	10.897610	22.1	22.2	21.6	2182	592
WISP1437-0149	PAR66-00029	20	M7	219.364258	-1.828590	21.4		21.6	1693	740
GOODSS0332-2755	GOODSS-05-G141_01783	13	M7	53.086269	-27.917154		22.1	22.1	2818	290
WISP1230+8236	PAR228-00015	36	M7	187.697586	82.607900		20.2		1079	29
WISP2222+0937	PAR50-00007	64	M7	335.595337	9.619006		19.7		845	22
WISP1847-6858	PAR134-00071	24	M7	281.901581	-68.969000			21.2	2013	49
WISP1419+0606	PAR345-00016	46	M7	214.868134	6.107460	20.8		20.7	1170	436
GOODSS0332-2751	GOODSS-06-G141_10354	57	M7	53.232479	-27.862617		20.5	20.4	1306	120
COSMOS1000+0217	COSMOS-12-G141_10098	54	M7	150.127716	2.283806		20.3	20.4	1251	138
GOODSN1236+6217	GOODSN-15-G141_29162	4	M7	189.171143	62.285847		25.1	24.8	10589	430
WISP1402+0946	PAR143-00045	11	M7	210.603149	9.769180	22.1		21.9	2052	717
WISP0914+4755	PAR299-00070	12	M7	138.669785	47.929800	22.7		22.4	2649	885
UDS0217-0513	UDS-15-G141_14762	17	M7	34.261978	-5.227352		21.9	21.9	2567	213
WISP0243-7211	PAR127-00028	33	M7	40.788712	-72.193700			20.7	1592	40
GOODSN1237+6210	GOODSN-43-G141_05553	78	M7	189.291306	62.168911		20.3	20.3	1219	131
WISP1005-2421	PAR336-00047	10	M7	151.336197	-24.362000	22.1		22.0	2173	834

**Table 2** continued on next page

**Table 2** (*continued*)

ShortName	GrismID	SNR_J	Spt	RA	DEC	F110W	F140W	F160W	Distance(pc)	Distance
WISP1410+2955	PAR222-00047	8	M7	212.553284	29.928500	22.1			2566	69
WISP0950+3544	PAR192-00026	18	M7	147.742004	35.734600	21.5			1896	50
GOODSN1236+6210	GOODSN-43-G141_05338	88	M7	189.236938	62.167187	20.0	19.9	1041	97	
UDS0217-0514	UDS-14-G141_11264	21	M7	34.419510	-5.239141	21.7	21.7	2300	217	
WISP2005-4140	PAR371-00100	7	M7	301.439331	-41.667000	22.6		22.5	2655	1004
GOODSS0333-2751	GOODSS-28-G141_12948	22	M7	53.288685	-27.851252	21.7	21.9	2429	329	
WISP1534+1252	PAR457-00025	16	M7	233.733124	12.881000	21.5		21.6	1713	697
WISP1348+2451	PAR243-00025	10	M7	207.047501	24.864700	21.7			2119	56
GOODSN1237+6215	GOODSN-36-G141_22694	47	M7	189.333832	62.252960	20.8	20.8	1558	158	
WISP1007+5013	PAR98-00038	21	M7	151.942719	50.227020		21.5	2312	59	
UDS0217-0515	UDS-14-G141_05410	31	M7	34.396893	-5.259149	21.3	21.2	1892	177	
WISP1545+1155	PAR290-00009	76	M7	236.311707	11.916900	19.2		655	18	
WISP1611+5221	PAR161-00061	11	M7	242.944473	52.355100		22.3	3449	87	
WISP1402+5410	PAR458-00004	107	M7	210.689911	54.173500	19.1		516	187	
WISP1225-0248	PAR38-00076	9	M7	186.307083	-2.805970	22.9	22.8	2862	655	
WISP2139-3824	PAR309-00023	29	M7	324.799408	-38.403000	21.2		1316	442	
WISP2005-4139	PAR371-00055	20	M7	301.420959	-41.655000	21.5		1415	385	
WISP1514+3617	PAR71-00034	10	M7	228.531723	36.291910	22.1		2071	741	
WISP1409+2621	PAR15-00041	12	M7	212.418945	26.350570	22.5	22.2	1897	546	
GOODSS0332-2750	GOODSS-19-G141_16588	35	M7	53.069553	-27.835718	21.2	21.1	1815	164	
GOODSN1236+6218	GOODSN-16-G141_33587	22	M7	189.242218	62.314220	21.8	21.8	2476	227	
WISP1323+3434	PAR186-00091	6	M7	200.928772	34.578900	22.2		2713	72	
WISP1256+5430	PAR110-00085	15	M7	194.249939	54.515200		22.4	3483	85	
WISP0948+1350	PAR427-00039	21	M7	147.228485	13.841600	22.4		2334	823	
UDS0217-0509	UDS-25-G141_36035	42	M7	34.340759	-5.155810	21.0	21.0	1718	170	
WISP0910+3328	PAR431-00028	11	M7	137.621338	33.466900	21.5		1583	576	
WISP1427+2631	PAR218-00032	13	M7	216.803177	26.519000	21.4		1850	50	
WISP1342+1841	PAR139-00010	70	M7	205.607071	18.696800		20.2	1301	32	
WISP1550+3959	PAR59-00072	13	M7	237.595795	39.991620	22.8		3439	93	
WISP0944-1941	PAR293-00059	8	M7	146.153305	-19.696000	21.9		2375	63	
AEGIS1418+5244	AEGIS-25-G141_18460	10	M7	214.742126	52.745266	22.8	22.8	3896	423	
WISP2345+1510	PAR77-00045	12	M7	356.250092	15.176390		21.7	2549	63	
GOODSS0332-2752	GOODSS-13-G141_07509	16	M7	53.123314	-27.874628	22.0	22.0	2711	245	
WISP2225-7212	PAR404-00044	15	M7	336.405060	-72.208000	21.9		1898	687	

**Table 2** continued on next page

**Table 2** (*continued*)

ShortName	GrismID	SNR_J	SPT	RA	DEC	F110W	F140W	F160W	Distance(pc)	Distance
WISP2040-0644	PAR248-00079	17	M7	310.109924	-6.737800	21.6			2042	55
AEGIS1419+5253	AEGIS-06-G141_12749	10	M7	214.981369	52.892410	22.6	22.5		3431	269
UDS0217-0513	UDS-09-G141_17647	21	M7	34.317680	-5.217520	21.6	21.6		2268	243
UDS0217-0513	UDS-15-G141_15337	160	M7	34.263683	-5.226482	19.0	19.0		667	66
WISP1009+3000	PAR39-00033	10	M7	152.409225	30.012280	21.7	22.0	21.1	1831	567
GOODSS0332-2745	GOODSS-09-G141_32414	17	M7	53.080120	-27.762650	22.3	22.1		2945	213
WISP1832+5344	PAR124-00053	18	M7	278.104370	53.743200	21.9		21.8	1935	729
WISP0926+1239	PAR92-00011	27	M7	141.534668	12.664310			20.7	1634	39
WISP0947+5126	PAR478-00038	17	M7	146.750015	51.442600	22.3		21.6	1964	532
WISP1410+2954	PAR222-00091	4	M7	212.550674	29.914000		23.1		4132	112
GOODSN1236+6209	GOODSN-21-G141_04680	11	M7	189.057877	62.161026	22.5	22.5		3334	338
WISP0455-2201	PAR194-00039	7	M8	73.960762	-22.023700		22.2		2327	31
WISP1023+0409	PAR347-00037	14	M8	155.843643	4.164820	22.2		22.0	1825	765
WISP0137-0908	PAR317-00032	17	M8	24.328993	-9.148480	21.7		21.1	1312	467
WISP0502+0732	PAR189-00077	7	M8	75.559814	7.535803		22.2		2397	31
UDS0217-0514	UDS-10-G141_10211	46	M8	34.368454	-5.242865		20.7	20.7	1309	111
WISP1500+4127	PAR391-00011	33	M8	225.079330	41.457200	20.9		20.7	1030	433
COSMOS1000+0222	COSMOS-25-G141_19163	9	M8	150.107285	2.374017		22.5	22.3	2902	195
WISP1514+3616	PAR71-00038	13	M8	228.548965	36.277920	22.2		21.6	1623	572
GOODSS0332-2742	GOODSS-30-G141_44380	74	M8	53.100697	-27.703068		20.1	20.1	987	89
WISP1604+1445	PAR240-00058	8	M8	241.243622	14.766600		22.4		2586	33
WISP0908+3246	PAR417-00014	30	M8	137.048172	32.776600	20.8		20.3	874	321
WISP1351+2751	PAR444-00034	16	M8	207.753510	27.852400	21.8		21.5	1476	599
WISP1427+2631	PAR218-00035	10	M8	216.796814	26.531400		21.5		1719	22
WISP1224+6110	PAR422-00021	30	M8	186.109833	61.182500		21.4		1584	20
WISP2335-3536	PAR359-00007	58	M8	353.832611	-35.602000	19.9		19.6	619	252
COSMOS1000+0227	COSMOS-08-G141_26927	13	M8	150.126282	2.459579		22.0	21.9	2306	187
UDS0217-0510	UDS-23-G141_31620	9	M8	34.259209	-5.170456		22.7	22.7	3301	396
WISP2131-1202	PAR342-00050	6	M8	322.946167	-12.045000	22.9		22.6	2462	993
WISP1547+2057	PAR335-00113	7	M8	236.926895	20.951200	23.3		23.0	3021	1207
WISP2038-2021	PAR197-00054	12	M8	309.592621	-20.363000		21.1		1411	18
WISP1604+1446	PAR240-00051	10	M8	241.234528	14.782200		22.2		2392	31
GOODSN1237+6219	GOODSN-27-G141_34168	20	M8	189.308624	62.318092		21.8	21.8	2163	229
WISP1006-2953	PAR171-00081	13	M8	151.730759	-29.894000			21.9	2532	26

**Table 2** continued on next page

**Table 2** (*continued*)

ShortName	GrismID	SNR_J	SPT	RA	DEC	F110W	F140W	F160W	Distance(pc)	Distance
WISP2139-3824	PAR309-00046	9	M8	324.795837	-38.402000	22.3		22.4	2127	991
WISP1125+5319	PAR477-00009	32	M8	171.342133	53.331300	20.8		20.4	923	362
WISP1605+2547	PAR148-00044	21	M8	241.354004	25.794100			21.9	2543	25
WISP1427+2352	PAR346-00021	29	M8	216.753586	23.878400	21.0		20.9	1110	503
WISP1554+3623	PAR72-00048	10	M8	238.697281	36.397810	22.3	22.3	22.2	2182	773
WISP0959+5549	PAR246-00017	21	M8	149.789856	55.820400			20.9	1292	16
GOODSS0332-2747	GOODSS-02-G141_24465	13	M8	53.075794	-27.796272		22.3	22.2	2675	247
WISP0911+1832	PAR271-00055	10	M8	137.887695	18.541900	22.2		21.8	1769	672
WISP0854+4351	PAR319-00085	7	M8	133.500824	43.853300	23.2		22.9	2841	1130
WISP0122-2838	PAR128-00052	14	M8	20.687748	-28.646200			22.3	3040	31
WISP1112+3536	PAR44-00044	19	M8	168.058868	35.607950	21.6	22.2	21.6	1765	680
WISP1006-2953	PAR170-00081	13	M8	151.730759	-29.894000			21.9	2531	25
WISP1432+0958	PAR428-00062	9	M9	218.003204	9.968530	22.2		22.0	1679	788
WISP1327+5248	PAR195-00023	14	M9	201.981293	52.809200			21.1	1270	16
WISP1007+1004	PAR343-00036	15	M9	151.918076	10.079000	21.5		21.2	1191	557
WISP1420+2541	PAR301-00036	11	M9	215.189285	25.691700			21.8	1770	23
WISP1605+1447	PAR240-00040	17	M9	241.256699	14.783400			22.0	1929	25
WISP0011-0653	PAR261-00027	25	M9	2.953725	-6.896139	21.1		21.2	1127	586
WISP1429+3224	PAR378-00052	8	L0	217.333206	32.416400	22.4		21.9	1527	683
WISP2333+3925	PAR153-00002	518	L0	353.414642	39.418100			15.7	128	2
WISP0246-0104	PAR483-00077	9	L0	41.721233	-1.079250	23.0		22.1	1741	643
WISP1618+3340	PAR65-00035	19	L0	244.707458	33.671520	21.7		21.3	1128	538
WISP1007+1004	PAR343-00083	6	L0	151.936081	10.079100	23.0		22.4	1921	810
WISP0248-3033	PAR313-00004	223	L0	42.134068	-30.552700	18.5		18.1	255	120
WISP2333+3922	PAR68-00017	146	L0	353.398834	39.370580	18.7		18.7	324	174
WISP2307+2111	PAR166-00004	326	L0	346.827850	21.193400			16.6	190	3
WISP0015-7955	PAR244-00072	6	L1	3.785810	-79.930220			22.2	1684	43
WISP1150-2033	PAR199-00009	57	L1	177.706833	-20.561000			19.2	417	11
UDS0217-0509	UDS-25-G141_36758	31	L1	34.318333	-5.153692		21.3	21.0	1196	91
WISP1154+1941	PAR338-00035	13	L1	178.716644	19.684700	22.2		21.9	1311	642
WISP1408+5657	PAR353-00055	13	L1	212.082855	56.956800	22.5		22.0	1376	620
GOODSN1236+6209	GOODSN-31-G141_04491	5	L2	189.082870	62.159412		24.3	24.1	3977	450
GOODSN1236+6211	GOODSN-33-G141_09283	12	L2	189.223923	62.188259		22.2	22.0	1508	136
WISP1133+0328	PAR27-00036	10	L2	173.274353	3.477643	21.6	22.0	21.4	990	394

**Table 2** *continued on next page*

**Table 2** (*continued*)

ShortName	GrismID	SNR_J	Spt	RA	DEC	F110W	F140W	F160W	Distance(pc)	Distance(kpc)
WISP1154+1939	PAR338-00136	4	L3	178.720154	19.660000	24.1		23.1	1692	525
WISP1544+4844	PAR54-00072	6	L3	236.225174	48.738480		22.9		1513	48
GOODSS0332-2749	GOODSS-20-G141_19648	6	L4	53.103283	-27.820263		23.2	23.2	1647	221
WISP0927+6027	PAR21-00005	324	L4	141.989319	60.462970		18.6		165	5
GOODSS0333-2751	GOODSS-28-G141_10859	34	L4	53.267498	-27.860249		21.4	21.3	700	105
WISP0125-0001	PAR365-00156	4	L4	21.396976	-0.027310	5.6		24.2	1529	1530
GOODSN1236+6209	GOODSN-32-G141_05180	4	L4	189.159195	62.164200		24.2	24.1	2591	340
WISP1625+5721	PAR156-00041	19	L4	246.353882	57.357600			21.4	824	23
COSMOS1000+0219	COSMOS-03-G141_14879	6	L4	150.093170	2.331386		23.2	23.0	1599	178
WISP1004+5258	PAR438-00051	10	L4	151.204559	52.974800		22.6		1076	33
GOODSN1236+6214	GOODSN-24-G141_21552	19	L4	189.161880	62.247669		22.0	21.8	915	102
GOODSS0332-2754	GOODSS-14-G141_01979	6	L4	53.209110	-27.913748		24.9	24.9	3726	653
GOODSN1235+6211	GOODSN-11-G141_10603	6	L5	188.967987	62.194958		23.3	23.0	1352	131
WISP2133-4904	PAR133-00012	87	L5	323.482574	-49.083000			19.6	304	7
WISP1124+4202	PAR106-00047	11	L6	171.034760	42.042900			21.5	626	10
WISP0105+0215	PAR231-00012	89	L8	16.310194	2.257870		18.9		123	0
UDS0217-0509	UDS-23-G141_32939	4	L9	34.250679	-5.165653		23.9	23.7	1343	164
COSMOS1000+0217	COSMOS-23-G141_10232	5	T0	150.145950	2.283675		23.8	23.8	1333	181
WISP1003+2854	PAR191-00077	6	T0	150.918884	28.912800			23.1	1096	9
UDS0217-0514	UDS-12-G141_10759	9	T0	34.435657	-5.240000		25.2	25.2	2637	390
WISP1019+2743	PAR201-00044	4	T1	154.888565	27.720400		22.4		574	5
WISP1115+5257	PAR468-00163	5	T1	168.809311	52.951400	24.3		24.4	1218	699
WISP0326-1643	PAR467-00135	3	T1	51.511295	-16.722500	23.9		23.9	988	556
WISP1150-2033	PAR199-00124	6	T1	177.704559	-20.565000		23.2		813	9
WISP0437-1106	PAR463-00176	4	T3	69.490608	-11.104400	24.3		24.3	924	352
GOODSS0332-2749	GOODSS-04-G141_17402	13	T3	53.161709	-27.831562		22.6	22.9	573	101
WISP0307-7243	PAR130-00092	12	T4	46.921608	-72.732600			22.7	455	21
AEGIS1418+5242	AEGIS-03-G141_17053	21	T4	214.710007	52.716480		22.7	23.1	473	71
GOODSS0332-2741	GOODSS-01-G141_45889	31	T6	53.242542	-27.695446		22.1	22.9	244	43
WISP1232-0033	PAR58-00112	11	T8	188.176712	-0.551850		23.1		562	69
WISP1305-2538	PAR32-00075	11	T9	196.356232	-25.641300	23.1	23.0	22.7	1537	1165

## REFERENCES

**Table 3.** Polynomial relations used in this work given by  $y = \sum_{n=1}^7 c_n x^n$ 

x	y	Scatter	Coefficients						
			c7	c6	c5	c4	c3	c2	c1
SpT	AbsF110W	-2E-06	4E-04	-2.8E-02	1.	-20.	203.	-846.	
SpT	AbsF140W	1E-06	-3.4E05	-9.8E-04	1.5e-01	-5.	72.	-381	
SpT	AbsF160W		-1E-02	2.9E-01	-8.	98.	-485.		
F110W	logSNR-J	0.40				-0.02	0.64	-2.2	
F140W	logSNR-J	0.43				0.01	-0.8,	12	
F160W	logSNR-J	0.43				0.002	-0.38	8.4	

**Table 4.** Number Densities (N) and effective volumes (V in pc<sup>3</sup>) for each scale height in pc. Nobs is the number of UCDs in the sample

SpT	N_100	N_1000	N_250	N_275	N_300	N_325	N_350	N_obs	V_100	V_1000	V_250	V_275	V_300	V_325	V_350
M7	1142.8	81.1	95.5	93.8	51.5	51.7	48.9	65	983052	124965	79851	74370	71283	69738	69237
M8	225.3	54	43.7	45.3	26	27.1	26.4	29	193823	83208	36486	35905	35988	36518	37366
M9	59.1	38.6	22.7	24.6	14.6	15.6	15.5	5	50829	59507	19009	19475	20159	21003	21971
L0	19.7	28.5	13.1	14.6	8.8	9.6	9.8	5	16916	43862	10938	11541	12241	13023	13876
L1	8	20.5	8.1	9.2	5.7	6.4	6.6	4	6841	31585	6786	7334	7943	8610	9329
L2	3.8	13.9	5.4	6.2	3.9	4.4	4.7	3	3237	21386	4477	4943	5454	6004	6589
L3	2	8.8	3.7	4.4	2.8	3.2	3.4	0	1734	13509	3110	3490	3896	4323	4765
L4	1.2	5.3	2.7	3.2	2	2.3	2.4	8	1024	8146	2238	2526	2824	3126	3427
L5	0.8	3.2	2	2.3	1.5	1.7	1.7	3	656	4893	1639	1842	2044	2241	2430
L6	0.5	2	1.5	1.7	1.1	1.2	1.2	1	451	3064	1218	1356	1489	1614	1731
L7	0.4	1.3	1.1	1.3	0.8	0.9	0.9	0	332	2074	934	1030	1120	1202	1278
L8	0.3	1	0.9	1	0.6	0.7	0.7	2	262	1548	754	826	892	952	1006
L9	0.3	0.8	0.8	0.9	0.5	0.6	0.6	1	222	1274	649	708	761	810	853
T0	0.2	0.7	0.7	0.8	0.5	0.5	0.5	3	200	1132	591	643	690	733	770
T1	0.2	0.7	0.7	0.8	0.5	0.5	0.5	2	192	1042	557	605	648	686	720
T2	0.2	0.6	0.6	0.7	0.4	0.5	0.5	0	191	941	526	567	605	638	667
T3	0.2	0.5	0.6	0.6	0.4	0.4	0.4	1	192	786	475	508	536	562	584
T4	0.2	0.4	0.5	0.5	0.3	0.3	0.3	2	187	578	392	413	430	446	459
T5	0.2	0.2	0.3	0.4	0.2	0.2	0.2	0	162	361	278	288	296	303	309
T6	0.1	0.1	0.2	0.2	0.1	0.1	0.1	1	110	182	156	159	162	164	166
T7	0.1	0	0.1	0.1	0	0	0	0	49	66	61	61	62	62	63
T8	0	0	0	0	0	0	0	1	12	15	14	14	14	14	15
Total	1465.6	262.2	204.9	212.6	122.2	127.9	125.3	136	1260674	404124	171139	168604	169537	172772	177611

- Atek, H., Malkan, M., McCarthy, P., et al. 2010, *\apj*, 723, 104
- Aumer, M., & Binney, J. 2009, *\mnras*, 397, 1286
- Bahcall, J., & Soneira, R. 1981, *\apjs*, 47, 357
- Baraffe, I., Chabrier, G., Allard, F., & Hauschildt, P. 2003, in IAU Symposium, Vol. 211, Brown Dwarfs, ed. E. Martín, 41–+
- Bardalez Gagliuffi, D., Burgasser, A., Gelino, C., et al. 2014, *\apj*, 794, 143
- Bardalez Gagliuffi, D. C., Burgasser, A. J., Schmidt, S. J., et al. 2019, arXiv e-prints, arXiv:1906.04166
- Basri, G. 1998, in Astronomical Society of the Pacific Conference Series, Vol. 134, Brown Dwarfs and Extrasolar Planets, ed. R. Rebolo, E. Martin, & M. Zapatero Osorio, 394–+
- Bate, M., Bonnell, I., & Bromm, V. 2002, *\mnras*, 332, L65
- Bate, M., Bonnell, I., & Bromm, V. 2003, in Astronomical Society of the Pacific Conference Series, Vol. 287, Galactic Star Formation Across the Stellar Mass Spectrum, ed. J. De Buizer & N. van der Blieck, 427–432
- Belokurov, V., Erkal, D., Evans, N. W., Koposov, S. E., & Deason, A. J. 2018, *MNRAS*, 478, 611
- Bertin, E., & Arnouts, S. 1996, *\aaps*, 117, 393
- Bochanski, J., Hawley, S., Covey, K., et al. 2010, *\aj*, 139, 2679
- Boubert, D., Guillochon, J., Hawkins, K., et al. 2018, *MNRAS*, 479, 2789
- Boubert, D., Guillochon, J., Hawkins, K., et al. 2018, *Monthly Notices of the Royal Astronomical Society*, 479, 2789–2795
- Brammer, G., van Dokkum, P., Franx, M., et al. 2012a, *\apjs*, 200, 13
- Brammer, G. B., van Dokkum, P. G., Franx, M., et al. 2012b, *The Astrophysical Journal Supplement Series*, 200, 13
- Bromm, V., & Loeb, A. 2003, *Nature*, 425, 812
- Burgasser, A. 2001, PhD thesis, AA(Department of Physics, California Institute of Technology)
- . 2004, *\apjs*, 155, 191
- . 2007, *\apj*, 659, 655
- . 2014a, ArXiv e-prints, arXiv:1406.4887
- Burgasser, A.,Looper, D., Kirkpatrick, J., & Liu, M. 2007, *\apj*, 658, 557
- Burgasser, A. J. 2014b, arXiv:1406.4887
- Burningham, B., Cardoso, C., Smith, L., et al. 2013, *\mnras*, 433, 457
- Burrows, A., Hubbard, W., Lunine, J., & Liebert, J. 2001, *Reviews of Modern Physics*, 73, 719
- Carnero Rosell, A., Santiago, B., dal Ponte, M., et al. 2019, arXiv e-prints, arXiv:1903.10806
- Chabrier, G. 2001, *\apj*, 554, 1274
- Chabrier, G., & Baraffe, I. 2000, *\araa*, 38, 337
- Chabrier, G., & Mera, D. 1997, *A&A*, 328, 83
- Collaboration, T. A., Robitaille, T. P., Tollerud, E. J., et al. 2013, arXiv:1307.6212
- Cruz, K., Reid, I., Kirkpatrick, J., et al. 2007, *\aj*, 133, 439
- Cushing, M., Tokunaga, A., & Kobayashi, N. 2000, *\aj*, 119, 3019

- Cushing, M., Kirkpatrick, J., Gelino, C., et al. 2011, *\apj*, 743, 50
- Davis, M., Guhathakurta, P., Konidaris, N. P., et al. 2007, *The Astrophysical Journal Letters*, 660, L1
- Day-Jones, A., Marocco, F., Pinfield, D., et al. 2013, *\mnras*, 430, 1171
- de Vaucouleurs, G., & Pence, W. D. 1978, *AJ*, 83, 1163
- Delfosse, X., Tinney, C. G., Forveille, T., et al. 1999, *Astron. Astrophys. Suppl. Ser.*, 135, 41
- Downes, J. J., Briceño, C., Mateu, C., et al. 2014, *MNRAS*, 444, 1793
- Dupuy, T., & Liu, M. 2012, *\apjs*, 201, 19
- Faherty, J. K., Bochanski, J. J., Gagne, J., et al. 2018, *The Astrophysical Journal*, 863, 91
- Filippazzo, J. C., Rice, E. L., Faherty, J., et al. 2015, *Astrophysical Journal*, 810, 158
- Freeman, K. C. 1987, *ARA&A*, 25, 603
- Gagné, J., Faherty, J. K., Cruz, K. L., et al. 2015, *arXiv:1506.07712*
- Gaia Collaboration, Brown, A. G. A., Vallenari, A., et al. 2018, *A&A*, 616, A1
- Gallart, C., Bernard, E. J., Brook, C. B., et al. 2019, *Nature Astronomy*, doi:10.1038/s41550-019-0829-5
- Giavalisco, M., Ferguson, H. C., Koekemoer, A. M., et al. 2004, *The Astrophysical Journal*, 600, L93
- Gould, A., Bahcall, J., & Flynn, C. 1997, *\apj*, 482, 913
- Grogin, N. A., Kocevski, D. D., Faber, S. M., et al. 2011, *ApJS*, 197, 35
- Hardegree-Ullman, K. K., Cushing, M. C., Muirhead, P. S., & Christiansen, J. L. 2019, *arXiv e-prints*, arXiv:1905.05900
- Hayashi, C., & Nakano, T. 1963, *Progress of Theoretical Physics*, 30, 460
- Haywood, M., Di Matteo, P., Lehnert, M., Katz, D., & Gómez, A. 2013, *\aap*, 560, A109
- Helmi, A., Babusiaux, C., Koppelman, H. H., et al. 2018, *Nature*, 563, 85
- Holwerda, B. W., Trenti, M., Clarkson, W., et al. 2014, *The Astrophysical Journal*, 788, 77
- Hunter, J. D. 2007, *Computing in Science Engineering*, 9, 90
- Ivezić, Ž., Beers, T. C., & Jurić, M. 2012, *ARA&A*, 50, 251
- Jones, E., Oliphant, T., Peterson, P., et al. 2001–, SciPy: Open source scientific tools for Python, , [Online; accessed 1 today]
- Jurić, M., Ivezić, Ž., Brooks, A., et al. 2008, *\apj*, 673, 864
- Kerins, E. J. 1997, *A&A*, 328, 5
- Kiman, R., Schmidt, S. J., Angus, R., et al. 2019, *AJ*, 157, 231
- Kimble, R. A., MacKenty, J. W., O'Connell, R. W., & Townsend, J. A. 2008, *Wide Field Camera 3: a powerful new imager for the Hubble Space Telescope*, , doi:10.1117/12.789581
- Kirkpatrick, J. 2005, *\araa*, 43, 195

- Kirkpatrick, J., Looper, D., Burgasser, A., et al. 2010, *\apjs*, 190, 100
- Kirkpatrick, J., Cushing, M., Gelino, C., et al. 2011, *\apjs*, 197, 19
- Kirkpatrick, J. D., Reid, I. N., Liebert, J., et al. 2000, *The Astronomical Journal*, 120, 447
- Kirkpatrick, J. D., Martin, E. C., Smart, R. L., et al. 2019, *ApJS*, 240, 19
- Koekemoer, A. M., Faber, S. M., Ferguson, H. C., et al. 2011, *ApJS*, 197, 36
- Koppelman, H. H., Helmi, A., Massari, D., Price-Whelan, A. M., & Starkenburg, T. K. 2019, arXiv e-prints, arXiv:1909.08924
- Kümmel, M., Walsh, J. R., Pirzkal, N., Kuntschner, H., & Pasquali, A. 2009, *Publications of the Astronomical Society of the Pacific*, 121, 59
- Kuntschner, H., Kümmel, M., & Walsh, J. R. 2013
- Laughlin, G., Bodenheimer, P., & Adams, F. 1997, *\apj*, 482, 420
- Lawrence, A., & Others. 2007, *\mnras*, 379, 1599
- Leggett, S. K., Ruiz, M. T., & Bergeron, P. 1998, *ApJ*, 497, 294
- Lodieu, N., Espinoza Contreras, M., Zapatero Osorio, M. R., et al. 2017, *Astronomy & Astrophysics*, 598, A92
- Lodieu, N., Burningham, B., Day-Jones, A., et al. 2012, *A&A*, 548, A53
- Lopez-Santiago, J., Montes, D., Crespo-Chacon, I., & Fernandez-Figueroa, M. J. 2006, *The Astrophysical Journal*, 643, 1160
- LSST Science Collaboration, L. S., Abell, P. A., Allison, J., et al. 2009, arXiv:0912.0201
- Luhman, K. L., & Mamajek, E. E. 2012, *The Astrophysical Journal*, 758, 31
- Malhan, K., Ibata, R. A., & Martin, N. F. 2018, *MNRAS*, 481, 3442
- Mamajek, E. E. 2015, *Proceedings of the International Astronomical Union*, 10, 21
- Manjavacas, E., Apai, D., Zhou, Y., et al. 2018, arXiv:1812.03963
- Marocco, F., Jones, H. R. A., Day-Jones, A. C., et al. 2015, *Monthly Notices of the Royal Astronomical Society*, 449, 3651
- Martin, E. C., Mace, G. N., McLean, I. S., et al. 2017, *The Astrophysical Journal*, 838, 73
- Masters, D., McCarthy, P., Burgasser, A., et al. 2012, *\apjl*, 752, L14
- Metchev, S., Kirkpatrick, J., Berriman, G., & Looper, D. 2008, *\apj*, 676, 1281
- Miller, A. A., Kulkarni, M. K., Cao, Y., et al. 2017, *The Astronomical Journal*, 153, 73
- Momcheva, I. G., Brammer, G. B., van Dokkum, P. G., et al. 2016, *The Astrophysical Journal Supplement Series*, 225, 27
- Myeong, G. C., Evans, N. W., Belokurov, V., Sand ers, J. L., & Koposov, S. E. 2018, *ApJL*, 856, L26
- Myeong, G. C., Vasiliev, E., Iorio, G., Evans, N. W., & Belokurov, V. 2019, *MNRAS*, 488, 1235
- Pedregosa, F., Varoquaux, G., Gramfort, A., et al. 2012, arXiv e-prints, arXiv:1201.0490

- Pirzkal, N., Sahu, K., Burgasser, A., et al. 2005, \apj, 622, 319
- Pirzkal, N., Burgasser, A., Malhotra, S., et al. 2009, \apj, 695, 1591
- Reid, I., Kirkpatrick, J., Liebert, J., et al. 1999, \apj, 521, 613
- Reylé, C. 2018, Astronomy & Astrophysics, 619, L8
- Reyle, C., Delorme, P., Willott, C. J., et al. 2010, Astronomy and Astrophysics, Volume 522, id.A112, 15 pp., 522, arXiv:1008.2301
- Rujopakarn, W., Eisenstein, D. J., Rieke, G. H., et al. 2010, ApJ, 718, 1171
- Ryan, R. E., Thorman, P. A., Yan, H., et al. 2011, The Astrophysical Journal, 739, 83
- Ryan, R. E., Thorman, P. A., Schmidt, S. J., et al. 2017, The Astrophysical Journal, 847, 53
- Ryan Jr., R., Hathi, N., Cohen, S., & Windhorst, R. 2005, \apjl, 631, L159
- Ryan Jr., R. E., & Reid, I. N. 2016, The Astronomical Journal, 151, 92
- Salvatier, J., Wiecki, T. V., & Fonnesbeck, C. 2016, PeerJ Computer Science, 2, e55
- Schmidt, S., West, A., Bochanski, J., Hawley, S., & Kielty, C. 2014, \pasp, 126, 642
- Schmidt, S., West, A., Hawley, S., & Pineda, J. 2010, \aj, 139, 1808
- Schneider, A. C., Cushing, M. C., Kirkpatrick, J. D., et al. 2015, The Astrophysical Journal, 804, 92
- Scoville, N., Aussel, H., Brusa, M., et al. 2007, The Astrophysical Journal Supplement Series, 172, 1
- Skelton, R. E., Whitaker, K. E., Momcheva, I. G., et al. 2014, The Astrophysical Journal Supplement Series, 214, 24
- Skrzypek, N., Warren, S. J., & Faherty, J. K. 2016, A&A, 589, A49
- Sorahana, S., Nakajima, T., & Matsuoka, Y. 2018, arXiv:1811.07496
- Spergel, D., Gehrels, N., Baltay, C., et al. 2015, arXiv:1503.03757
- Theissen, C. A., West, A. A., Shippee, G., Burgasser, A. J., & Schmidt, S. J. 2017, AJ, 153, 92
- Tokunaga, A., & Kobayashi, N. 1999, \aj, 117, 1010
- Tolstoy, E., Hill, V., & Tosi, M. 2009, ARA&A, 47, 371
- Van Vledder, I., Van Der Vlugt, D., Holwerda, B. W., et al. 2016, Monthly Notices of the Royal Astronomical Society, 458, 425
- Virtanen, P., Gommers, R., Oliphant, T. E., et al. 2019, arXiv e-prints, arXiv:1907.10121
- Waskom, M., Botvinnik, O., Hobson, P., et al. 2014, seaborn: v0.5.0 (November 2014), v.v0.5.0, Zenodo, doi:10.5281/zenodo.12710
- York, D., & Others. 2000, \aj, 120, 1579